An Analysis of the Factors Influencing the Capacity of Constrained Urban Airspace

Thesis Paper

Michiel Aarts

Technische Universiteit Delft

TU Delft

An Analysis of the Factors Influencing the Capacity of Constrained Urban Airspace

Thesis Paper

by

Michiel Aarts

June 30th, 2021

to obtain the degree of Master of Science
at the Delft University of Technology,
to be defended publicly on Thursday July 15th, 2021 at 11:00 AM.

Student number: 4298446
Project duration: September 10, 2020 – July 15, 2021
Supervisors: Prof. dr. ir. J. M. Hoekstra*
Dr. ir. J. Ellerbroek*
Dr. V. L. Knoop‡

*Department of Control & Simulation, Faculty of Aerospace Engineering, Delft University of Technology
‡Department of Transport & Planning, Faculty of Civil Engineering and Geosciences, Delft University of Technology
Cover image obtained from https://www.nasa.gov/aero/taking-air-travel-to-the-streets-or-just-above-them/ on 08-12-2020, Credits: NASA / Lillian Gipson

TU Delft

Abstract

The traffic density of small aerial vehicles operating within urban environments is expected to increase significantly in the near future. This urban environment is highly constrained due to being limited to the low-altitude airspace directly above the existing road network. To increase understanding of the factors influencing the capacity of urban airspace, multiple empirical studies have been performed using fast-time simulations. However, the empirical nature of these simulations hampers the extrapolation of their results beyond the specific conditions that have been tested. At the same time, the emergent behaviour of aircraft in constrained urban airspace, such as queueing and local hotspots, yields the existing analytical models for general airspace invalid. In this paper, we derive and validate an analytical model approximating the relationship between the mean flow rate and mean density in a two-dimensional orthogonal grid network airspace, expressed in the so-called Macroscopic Fundamental Diagram. This analytical model is based on road transportation queueing theory and can explain the different interactions occurring in constrained urban airspace compared to general airspace. Notable findings show that the entire airspace can become unstable when the maximum capacity of a single intersection only is reached. Furthermore, the maximum airspace density is found to be unaffected by cruise speed. The results demonstrate how the derived analytical model for the Macroscopic Fundamental Diagram provides an increased understanding of the factors that influence capacity of constrained urban airspace, thereby offering an effective tool for urban airspace design applications. Moreover, this model lays the groundwork for the derivation of more expanded models, including the altitude dimension and non-orthogonal or non-four-way intersections, that can further improve comprehension of constrained urban airspace.

Keywords – Constrained urban airspace; Decentralised airspace; Speed-based conflict resolution; Analytical model; Airspace capacity; Airspace stability; Macroscopic Fundamental Diagram; Urban Traffic Management (UTM); BlueSky ATM simulator

1. Introduction

In recent years, the development of unmanned aerial vehicles (UAVs) and personal aerial vehicles (PAVs) has been proposed as a solution for the increasing number of road congestion problems within cities. Doole et al. [4] estimated that, even for a conservative growth rate, the traffic density of parcel and food delivery UAVs in the urban airspace of Paris would reach more than 60 thousand by 2035. These numbers are substantially higher than predicted regular, en-route airspace densities (Hoekstra et al. [11]). Furthermore, the environment of the low-altitude urban airspace is highly constrained. Flying above existing infrastructures, such as roads and waterways, is desired to reduce exposure to the urban population (Doole et al. [5], Salleh et al. [22]) or even unavoidable due to the presence of high buildings in the low-altitude urban airspace. The high level of aircraft density and the increased level of constraints are not found in regular, en-route airspace, raising the question of how and whether the constrained urban airspace can sustain such densities.

To answer this question, multiple studies have investigated the effect of the structure of an airspace on its capacity. The 'Metropolis' project (Sunil et al. [23, 24]) concluded that non-constrained airspace capacity benefits from partly constraining traffic by adding altitude layers with a limited heading range. This vertical segmentation was confirmed to be beneficial as well for the constrained urban airspace by Doole et al. [5], who also demonstrated the advantages of structuring the constrained urban airspace into one-way airways versus two-way airways. Similarly, Salleh et al. [21] argued that a structured airspace design is a prerequisite to enable large scale urban airspace operations, with follow-up research showing that the airspace should not be overly constrained (Salleh et al. [22]). In all studies mentioned, fast-time simulations are used to compare the different concepts for airspace structure.

However, the empirical nature of the fast-time simulations used in these studies hampers the extrapolation of their results beyond the specific conditions tested (Sunil et al. [27]). As a result, comprehension of the interactions between all parameters is limited. Simultaneously, further knowledge on the effects of the high level of constraints in the low-altitude airspace is desired. Developing a mathematical model using an analytical approach can quantify the factors influencing capacity of constrained urban airspace, increasing understanding. For that reason, an analytical model was proposed in follow-up research to the Metropolis project to predict capacity of non-constrained airspace quantitatively (Sunil et al. [25, 26]).

Still, the existing analytical models derived by Sunil et al. [25, 26] for non-constrained airspace are not valid for constrained urban airspace, as the constraints affect aircraft behaviour. For example, in a constrained environment, the limited horizontal manoeuvre space prevents horizontal resolution

manoeuvres. Moreover, when traffic is stacked in altitude layers of different speed or heading directions, as advocated by Doole et al. [5], Jang et al. [14], Sunil et al. [23, 24], vertical resolution possibilities are limited. As a result, of the three available en-route conflict resolution options (Kuchar and Yang [17]), only speed-based algorithms are feasible in constrained urban airspace. Simultaneously, pre-departure conflict resolution, also called take-off resolution, is assumed too restrictive in constrained airspace, as all aircraft need to pass through a limited number of intersections and airways. Therefore, this paper assumes tactical, en-route conflict resolution to be performed using speed-based algorithms.

An emergent behaviour resulting from speed-based resolution manoeuvres in a constrained environment is that aircraft queue upstream of busy intersections. In other words, within an airway, an aircraft can be in continuous conflict with the aircraft directly in front, yielding conflict count models less valuable. Furthermore, as concluded by Sunil et al. [27], the accuracy of their earlier proposed analytical model (Sunil et al. [26]) degrades when creating artificial 'hotspots' with a higher traffic density. Constrained urban airspace is a clear example of an environment with many hotspots, as traffic becomes concentrated on busy streets and intersections. Altogether, the existing analytical models are not valid for constrained urban airspace, signifying the need for a tailored analytical model.

While constrained urban airspace has different characteristics than non-constrained airspace, it has many similarities with road transportation environments. Hence, road transportation research can assist in modelling the constrained urban airspace. Although road transportation research seldom considers conflicts and conflict resolutions, network efficiency and instability are extensively investigated. Recent research in urban road transportation has focused on the relationship between the mean flow rate and the mean density in a network (Daganzo et al. [2], Gayah and Daganzo [8], Geroliminis and Daganzo [9], Knoop et al. [16]). This relationship is expressed in the so-called Macroscopic Fundamental Diagram (MFD), which Geroliminis and Daganzo [9] experimentally confirmed to exist in Yokohoma, Japan. Using the MFD, the behaviour of a road network can be observed, such that the traffic status (free-flow or congestion), critical density, and efficiency are identified (Jang et al. [14]). As aircraft behaviour shows many similarities to road traffic behaviour in constrained urban environments, the Macroscopic Fundamental Diagram is a useful metric to assess constrained urban airspace as well.

This study aims to increase understanding of the factors influencing the capacity of constrained urban airspace. Therefore, an analytical method is developed to estimate the relationship between the mean flow rate and the mean density, expressed in the Macroscopic Fundamental Diagram, for a two-dimensional, orthogonal grid network airspace. The derived model provides an effective tool for urban airspace design applications. Furthermore, this study lays the groundwork for the derivation of more expanded models, enabling an increased comprehension of the constrained urban airspace.

This paper continues by presenting background material in Section 2. Subsequently, Section 3 elaborates on the interactions between aircraft in a constrained urban environment, paving the way for the derivation of the analytical model. The analysis of the interactions shows that, to approximate the Macroscopic Fundamental Diagram, an analytical delay model is required, which is derived in Section 4. Next, using three fast-time simulation experiments, the level of accuracy of the analytical model is assessed. The experimental setup is discussed in Section 5, and the empirical results of these fast-time simulation experiments are compared to the predictions of the analytical model in Section 6. In Section 7, we discuss the level of accuracy of the derived model, the limitations, and the key findings, next to outlining the limitations of this study. Additionally, opportunities for future research are presented. Finally, the main conclusions are summarised in Section 8.

2. Background

In this section, background material is provided regarding conflicts, intrusions, and the tactical conflict resolution methods used in this paper. Next, a short review is presented of the analytical models already existing in road transportation literature to approximate the Macroscopic Fundamental Diagram, substantiating the motivation behind the derivation of a new model tailored to the constrained urban airspace.

2.1. Conflicts and intrusions

An *intrusion*, also called loss of separation, occurs when two aircraft simultaneously violate the minimum horizontal and vertical separation requirements. In this paper, an aircraft is assumed to be any small flying vehicle with hovering capabilities, e.g., UAVs, PAVs, or helicopters. When an intrusion

is predicted to occur within a predetermined look-ahead time, this is called a *conflict*. The difference between conflicts and intrusions is shown in Figure 1. By definition, conflicts and intrusions are pairwise, i.e., between two aircraft only.

(a) Conflict (b) Intrusion

Figure 1: The difference between a conflict, i.e., a predicted, future intrusion, and an intrusion in the horizontal plane, with S_h the horizontal separation requirement

To prevent intrusions, most research in urban airspace either makes use of pre-departure separation (Peinecke and Kuenz [19], Salleh et al. [22]) or of en-route decentralised air traffic management (ATM) performed by each aircraft autonomously (Doole et al. [5], Sunil et al. [23, 24]). A decentralised ATM system is often assumed in high-density urban airspace, as the current centralised ATM system already becoming saturated (Hoekstra et al. [11]). This paper uses decentralised ATM with en-route conflict resolution, as pre-departure separation is assumed too restrictive for constrained environments. Hence, to maintain an acceptable level of safety, a system to detect and resolve conflicts needs to be in place.

In this study, state-based *conflict detection* and speed-based *conflict resolution* are assumed. With state-based conflict detection, aircraft positions are linearly extrapolated along the velocity vector for a given look-ahead time. When within this look-ahead time an intrusion will take place, this is detected as a conflict. Note that, when using state-based detection, turns are not predicted. It is assumed that aircraft have perfect knowledge of their own and others' states. In reality, the accuracy of this state information can be considered in the design choice for the horizontal and vertical separation requirements, to prevent inaccuracies from resulting in collisions.

Upon detection of a conflict, an aircraft will perform tactical conflict resolution to avoid the predicted intrusion. As mentioned in the introduction, of all three en-route conflict resolution algorithms available, only speed-based conflict resolution algorithms are feasible. The implementation of speed-based conflict resolution means that airways can be one-way only (per altitude level), as head-on conflicts are not resolvable.

Moreover, analogous to a road transportation network, it is likely that a speed limit will be set per airway and altitude. It is assumed that all aircraft will fly at equal cruise speed V_{NR} when no conflict resolution (NR) would be used, likely close to such a speed limit. Already, the FAA proposed a speed limit for small UAVs of 45m/s (Federal Aviation Administration [7]). In addition, the International Rules of the Air (International Civil Aviation Organization [13]) define that an overtaking aircraft has to give right-of-way to the aircraft being overtaken. Due to both reasons, the resolution of a conflict by accelerating is assumed infeasible in a two-dimensional constrained environment. Hence, the speed with resolution (WR) V_{WR} needs to be lower than the cruise speed. By assuming hovering capabilities for all aircraft, the lower bound equals 0, and the range of V_{WR} is:

$$V_{WR} \in [0, V_{NR}\rangle \tag{1}$$

2.2. Existing analytical models for the Macroscopic Fundamental Diagram

Two analytical models exist to approximate the Macroscopic Fundamental Diagram in an urban road transportation grid (Tilg et al. [28]): the method of cuts and the stochastic approximation method. Both existing analytical methods will not be used, as they are not directly translatable to the urban airspace. Due to the absence of a reaction time in the definition of the horizontal separation requirement, the 'congestion' branch is replaced by a hard density limit when the airway length equals the number of aircraft multiplied by the separation requirement. Moreover, both models are based on roads with traffic signals operating with a fixed cycle time. In this paper, no traffic signals are assumed.

Still, urban road transportation research does provide the starting point for the derivation of the analytical MFD model in this paper, in the form of the analytical delay model of Webster [29]. This delay model expresses the mean delay per vehicle at intersections with traffic signals. To adapt to the speed-based environment without traffic signals, Section 4 discusses several required modifications.

3. Aircraft interactions in a constrained environment

This section presents the different aircraft interactions existing in a two-dimensional constrained urban airspace environment. These interactions need to be considered to allow the derivation of an analytical model for the relationship between the mean flow rate and the aircraft density. At a single orthogonal intersection, two types of traffic are distinguished. *Through traffic* represents the set of aircraft that continues on a straight path, whereas *turning traffic* represents the set of aircraft that turns onto the other airway. This section starts by evaluating the effect of through traffic of two upstream flows crossing a single intersection. Next, the additional effect of turning traffic on a single intersection is analysed. Finally, the impact of speed-based conflict resolution on aircraft behaviour in an orthogonal grid network is examined. The emergent behaviour of the aircraft, including queueing for intersections, demonstrates the motivation for a delay model, which will be derived in Section 4.

3.1. Effect of alternating upstream legs

Consider an intersection of two one-way airways, with through traffic only. A difference exists in the minimum separation distance between two aircraft coming from the same upstream leg and between two aircraft coming from different upstream legs, see Figure 2.

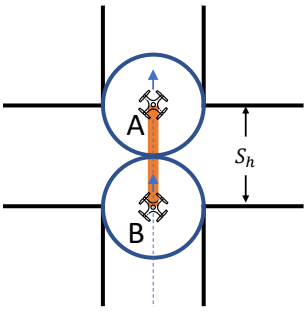

(a) Minimum separation distance $S_\parallel$ between subsequent aircraft coming from the same leg. $|\Delta\psi| = 0$ and the separation distance $S_\parallel = S_h$

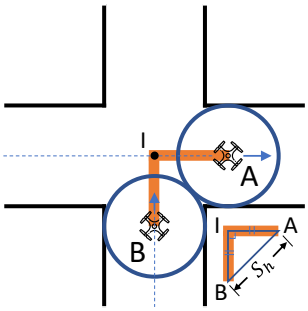

(b) Minimum separation distance S_+ between subsequent aircraft coming from alternating legs. Aircraft A originates from the west, while B originates from the south. $|\Delta\psi| = \pi/2$ and the time window $S_+ = S_h\sqrt{2}$

Figure 2: Minimum separation distance between aircraft on an intersection of two one-way airways, shown visually as the orange bar

In Figure 2a, to remain conflict-free, aircraft B must follow aircraft A at a distance of at least the horizontal separation requirement S_h. This safe distance is called the conflict-free flight distance $S_{h,\angle}$ and is geometrically defined as a function of the absolute difference in ground track angle $|\Delta\psi|$ at the intersection:

$$S_{h,\angle}(|\Delta\psi|) = \frac{S_h}{\cos(|\Delta\psi|/2)} \tag{2}$$

By using this equation, the minimum separation distance $S_\parallel$, shown as the orange bar in Figure 2a, between subsequent aircraft coming from the same leg can be determined:

$$S_\parallel = S_{h,\angle}(0) = S_h \tag{3}$$

In the situation where two aircraft originate from different upstream legs, the conflict-free flight distance increases. This situation is visualised in Figure 2b, where the orange bar represents the minimum separation distance S_+ for aircraft coming from different upstream legs. In this figure, the conflict-free flight distance is increased to the distance B→I→A, with I signifying the intersection midpoint. For an orthogonal intersection, by applying Equation (2), S_+ equals:

$$S_+ = S_{h,\angle}(\pi/2) = S_h\sqrt{2} \tag{4}$$

In summary, after a crossing aircraft of the other airway, the subsequent aircraft needs to keep a separation distance over the path of at least $S_h\sqrt{2}$. However, following a trough aircraft of its own airway, a margin of S_h suffices. Therefore, it is assumed that:

> Assumption 1: When the origin leg of the crossing traffic at an intersection alternates less often between both upstream legs, maximum capacity can be increased compared to an intersection with perfectly alternating upstream legs.

3.2. Effect of turning traffic

Consider an intersection of two one-way airways with turning traffic being present next to the through traffic. When turning traffic is present, a state-based conflict detection algorithm does not predict the turns. Two situations need to be considered that affect capacity: either (1) turning aircraft A is in the airway of aircraft B and turning onto the crossing airway, or (2) turning aircraft A is on the crossing airway and merging into the airway of aircraft B.

For the first case, aircraft B can follow aircraft A conflict-free at a distance of $S_\parallel$ of Equation (3) within the airway. As both aircraft have the same airspeed, no conflict is detected. However, after the turn of aircraft A, a similar situation as visualised in Figure 2b occurs, although aircraft A originated from the south instead of the west. As a result, aircraft B suddenly needs to keep a margin equivalent to S_+ of Equation (4). Hence, when the two aircraft were following each other more closely than S_+ within the airway, the leading aircraft A provoked a conflict with B by turning. Therefore, each aircraft trailing a turning aircraft within a distance S_+ needs to decelerate and increase its distance to S_+ to resolve the conflict. In other words, this case of turning traffic has an increasing effect on delay.

In the second situation, the difference with non-turning traffic is that the planned route of an aircraft, including a turn, results in the predicted intrusion being avoided. This is called a false conflict. With state-based conflict detection algorithms, aircraft cannot distinguish false conflicts from actual conflicts as long as the look-ahead time is sufficiently long. Therefore, aircraft try to resolve these false conflicts as well. In this situation, aircraft B decelerates to prevent the intrusion and to increase its distance to S_+. However, during the turn of aircraft A, the closest point of approach is moved away from aircraft B. After the turn, a situation comparable to the situation depicted in Figure 2a occurs, with aircraft A instead originating from the western leg. At this instant, the ground track angles of both aircraft are aligned, and the separation distance, previously considered to be S_+, can be reduced to $S_\parallel$. Therefore, the second case of turning traffic has a decreasing effect on delay.

When the flow rates from the upstream legs are approximately identical, the first situation occurs equally often as the second situation. In addition, the magnitude of change in separation distance is equal, with the sign being opposite. Hence, both effects counterbalance each other, resulting in the following assumption:

> Assumption 2: Through traffic and turning traffic have an equal impact on the mean intersection delay.

In this analysis, it is assumed that aircraft do not decelerate to perform a turn. If that is the case, additional delay needs to be modelled per turning aircraft and turning traffic will have an increased impact compared to through traffic. To prevent this additional delay, future airspace designs could implement solutions such as turning altitude layers (Doole et al. [5]), similar to turning lanes in road traffic.

3.3. Effect of conflict resolution in constrained urban airspace

In constrained urban airspace, three emergent properties due to speed-based conflict resolution need to be considered. These are an increase in density, a queueing effect, and a structuring effect. Firstly, the increase in density occurs as aircraft resolve a conflict by decelerating, thereby extending their flight time. This increase can be expressed analytically, starting from the (hypothetical) mean number of instantaneous aircraft without resolution $\overline{N}_{i,NR}$. $\overline{N}_{i,NR}$ and the mean flow rate $\overline{q}$ are related through the flight duration (which equals the mean flight distance $\overline{D}$ divided by the cruise speed V_{NR}):

$$\overline{N}_{i,NR} = \frac{\overline{D}}{V_{NR}}\overline{q}_{NR} \tag{5}$$

Aircraft routes and departure times are not impacted by the speed-based conflict resolution used in this paper. Therefore, in a stable situation, an equal number of aircraft depart, arrive or pass an intersection per unit time, regardless of whether or not conflict resolution is used. Hence, the mean flow rate $\overline{q}$ is unchanged, i.e., $\overline{q}_{NR} = \overline{q}_{WR}$. In addition, the mean airspeed with resolution can be extracted using the increased mean flight duration, which is the sum of the no resolution flight duration and the mean delay $\overline{d}$:

$$V_{WR} = \frac{\overline{D}}{\frac{\overline{D}}{V_{NR}} + \overline{d}} \tag{6}$$

Subsequently, the actual density, expressed as the mean number of instantaneous aircraft with resolution $\overline{N}_{i,WR}$, is given by substituting V_{NR} with V_{WR} of Equation (6) into Equation (5):

$$\overline{N}_{i,WR} = \frac{\overline{D}}{V_{WR}}\overline{q}_{NR} = \left(\frac{\overline{D}}{V_{NR}} + \overline{d}\right)\overline{q}_{NR} \tag{7}$$

The mean route length $\overline{D}$, the cruise speed V_{NR}, and the mean flow rate q_{NR} are assumed known input variables. Thus, the mean delay $\overline{d}$ is the only unknown variable required to obtain the mean density and, thereby, to express the entire Macroscopic Fundamental Diagram.

Secondly, within airways, a queueing effect can occur. While an aircraft waits for a crossing aircraft, other aircraft coming from upstream in the same airway approach the waiting aircraft and form a queue, increasing the density locally. When a queue gets longer, it can start to interfere with upstream intersections. This interference is visualised in Figure 3. In this figure, intersection A is operating above its capacity limit. As a result, not all aircraft can cross the intersection, blocking the aircraft in the northbound leg, with the queue overflowing to the upstream intersection B. In turn, this queue blocks all traffic in the westbound airway upstream of intersection B.

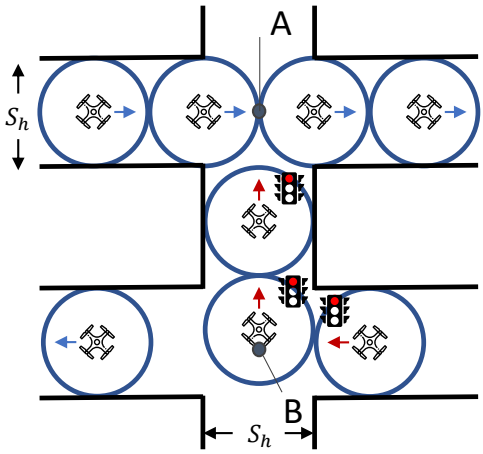

Figure 3: A small grid network experiencing overflow. Intersection A is operating above its capacity limit, leading to overflow blocking upstream intersection B

In other words, queueing has a destabilising effect on the network flows, as intersections become occupied by the queueing aircraft, blocking all flows at that intersection. Therefore, it is assumed that once a queue reaches an upstream intersection, the airspace becomes unstable:

> Assumption 3: Once the mean queue length within a leg of an intersection is longer than the distance to the upstream intersection of that leg, the airspace becomes unstable.

Due to the stochastic effects, the queue length varies and is longer than the mean length at particular intervals. As a result, the network can already become unstable at a lower flow rate than at the flow rate needed for the mean length of Assumption 3. The assumption is, therefore, expected to overestimate the instability density. Nevertheless, Assumption 3 is an effective metric to use as a theoretical

maximum capacity limit for a given constrained urban airspace, similar to the stability metric defined by Sunil et al. [25] for general airspace.

Thirdly, a structuring effect is present. During the delay of an aircraft, a queue forms behind this aircraft. When the intersection becomes free to cross, the queued aircraft continue their flight bunched together. In other words, aircraft get structured into *platoons* of multiple aircraft following each other closely. These platoons can impact the mean delay at downstream intersections. Namely, a platoon of multiple aircraft can either fit in a relatively tinier gap, decreasing the mean delay for the aircraft in the platoon, or be blocked entirely, increasing the mean delay for the platoon. However, structuring does not impact the mean flow rate as the number of aircraft does not change when measured over a long period. Furthermore, in this paper, traffic at the intersection adheres to the first-come, first-serve principle because no systems are present to limit flow alternation. Therefore, delay periods are limited to a single crossing aircraft, reducing the size of platoons. Altogether, the effect is assumed negligible for all densities:

> Assumption 4: The structuring effect has a negligible impact on the mean delay for all airspace densities.

4. Modelling delay in a constrained urban airspace

In this paper, the speed-based conflict resolution algorithm dictates that an aircraft resolves a conflict by decelerating for a particular period. This way, each conflict results in a delay incurred by a single aircraft. With an analytical delay model, the mean density in constrained urban airspace with conflict resolution can be approximated, yielding an expression for the Macroscopic Fundamental Diagram through Equation (7). As input variables, the mean flow rates $\overline{q}$ in each leg of the network are required, which can be determined when all aircraft routes and departure times are known. This section presents the derivation of an analytical delay model for a two-dimensional orthogonal grid network.

Consider the single, same-level, orthogonal intersection of area A of a northbound and an eastbound airway as shown in Figure 4. Turning onto the other airway is allowed. Therefore, across the intersection, four possible flows exist: an eastbound (E) through flow, a northbound (N) through flow, an east- to northbound (EN) turning flow, and a north- to eastbound (NE) turning flow. These are further grouped into a set U of the two upstream legs u, with mean flow rates $\overline{q}_E + \overline{q}_{EN}$ and $\overline{q}_N + \overline{q}_{NE}$, and a set D of the two downstream legs d, with mean flow rates $\overline{q}_E + \overline{q}_{NE}$ and $\overline{q}_N + \overline{q}_{EN}$, respectively. The set of all legs F represents the union of set U and D.

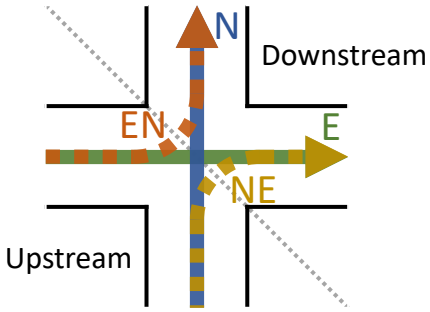

Figure 4: Orthogonal intersection of area A with two one-way airways and four flows: eastbound (E), northbound (N), east- to northbound turn (EN), and north- to eastbound turn (NE)

Such an intersection has many similarities with signalised intersections found in road transportation. Therefore, as a starting point in the derivation of the delay model, the signalised intersection delay model by Webster [29] will be used:

$$\overline{d} = \frac{c(1-\lambda)^2}{2(1-\lambda x)} + \frac{x^2}{2\overline{q}(1-x)} - \text{empirical correction factor } (\approx 5-15\%) \tag{8}$$

In this equation, the mean delay incurred in an upstream leg $\overline{d}$ is approximated by three terms. The first term models the general delay, which is incurred when traffic arrives at a red signal at a constant rate. The second term models the stochastic delay, representing the incurred delay due to the random nature

of the separation between consecutive arrivals. The third term is included to match the experimental road traffic data found by Webster [29]. In this paper, the empirical correction factor is not used, as this approximates specific road traffic behaviour. Therefore, the mean delay of aircraft in an upstream leg, $\overline{d}_u$ is given by the sum of the mean general delay $\overline{d}_{g,u}$ and the mean stochastic delay $\overline{d}_{s,u}$:

$$\overline{d}_u = \overline{d}_{g,u} + \overline{d}_{s,u} \tag{9}$$

First, the mean general delay in an upstream leg $\overline{d}_{g,u}$ is approximated. At the intersection of Figure 4, the maximum number of aircraft per unit time that can cross when the two flows are perfectly alternating is called the crossing flow capacity s_+ of the intersection. s_+ is defined as 1 aircraft per time t_+ a crossing aircraft needs to clear the intersection for the alternating leg completely. Without other conflicts, t_+ is given by:

$$t_+ = \frac{S_+}{V_{NR}} \tag{10}$$

Hence, for any two crossing flows flying at equal speed V_{NR}, s_+ is defined by:

$$s_+ = \frac{1}{t_+} = \frac{V_{NR}}{S_h\sqrt{2}} \tag{11}$$

Recall that the separation distance S_+ assumes that the flows are perfectly alternating. When the flows are not perfectly alternating, the mean distance decreases. Therefore, the time to cross t_+ is predicted to be underestimated at regular intersections.

In this paper, no traffic signal is used. Instead, the red signal time r used in the derivation of Webster's model can be interchanged by the time t_+ that the crossing aircraft occupies the intersection. This red time happens at a mean cycle time $\overline{c}_u$ equivalent to the mean time window between two consecutive aircraft of the crossing flow (i.e., the flow originating from the other upstream leg). This time window is inversely proportional to the mean crossing flow rate $\overline{q}_c$, meaning that:

$$r = t_+ \tag{12}$$

$$\overline{c}_u = 1/\overline{q}_c \tag{13}$$

Hence, the mean proportion of time $\overline{\lambda}$ that the traffic in an upstream leg u perceives the intersection to be free to cross, equals:

$$\overline{\lambda}_u = 1 - \frac{r}{\overline{c}_u} = 1 - t_+\overline{q}_c \tag{14}$$

When an intersection is free to cross, two aircraft coming from the same upstream leg can cross with a minimum separation time window equal to $t_\parallel$:

$$t_\parallel = \frac{S_\parallel}{V_{NR}} \tag{15}$$

Accordingly, the maximum airway flow capacity $s_\parallel$ is inversely proportional to $t_\parallel$:

$$s_\parallel = \frac{1}{t_\parallel} = \frac{V_{NR}}{S_h} \tag{16}$$

Lastly, the mean ratio of the actual flow to the maximum flow which can pass through an intersection from the upstream leg is called the degree of saturation $\overline{x}_u$ and is given by (Webster [29]):

$$\overline{x}_u = \frac{\overline{q}_u}{\lambda_u s_\parallel} \tag{17}$$

By substituting all variables defined above into the first part of Equation (8), the mean general delay $\overline{d}_g$ is obtained:

$$\overline{d}_{g,u} = \frac{\overline{c}_u(1-\overline{\lambda})^2}{2(1-\overline{\lambda}\overline{x})} = \frac{(1-t_+\overline{q}_c)^2}{2\overline{q}_c(1-t_\parallel\overline{q}_u)} \tag{18}$$

Next, the mean stochastic delay in an upstream leg $\overline{d}_{s,u}$ is derived. It concerns the flow within an airway, as it models the delay incurred due to queueing for a waiting aircraft. By inserting Equation (17) into the second part of Equation (8), the single intersection airspace version of $\overline{d}_{s,u}$ is obtained:

$$\overline{d}_{s,u} = \frac{\overline{x}_u{}^2}{2\overline{q}_u(1-\overline{x}_u)} \tag{19}$$

With expressions for both the mean general delay (Equation (18)) and the mean stochastic delay (Equation (19)), the mean delay incurred by an aircraft in an upstream leg can be determined using Equation (9). As aircraft in the downstream legs do not encounter any conflicts, no delay is incurred after crossing. Thus, the total mean intersection delay $\overline{d}_+$ is given by weighting the mean flow delays $\overline{d}_u$ with their respective mean flow rates $\overline{q}_u$ for both upstream legs u at the intersection:

$$\overline{q}_+ = \sum_{u \in U} \overline{q}_u \tag{20}$$

$$\overline{d}_+ = \frac{1}{\overline{q}_+} \sum_{u \in U} \overline{d}_u q_u \tag{21}$$

The goal of deriving a delay model is to approximate the relationship between the mean flow rate and the mean density, expressed in the Macroscopic Fundamental Diagram. The mean flow rate is a known input variable, meaning that through Equation (7) the mean density can be determined. By summing Equation (7) for each intersection leg f, the mean number of instantaneous aircraft with resolution at a single intersection $\overline{N}_{i,WR,+}$ can be derived to be:

$$\overline{N}_{i,WR,+} = \sum_{f \in F} \overline{N}_{i,WR,f} = \sum_{f \in F} \left(\frac{D_f}{V_{NR}} + \overline{d}_f \right) \overline{q}_f \tag{22}$$

By Assumption 2, Equations (21) and (22) are valid for intersections with and without turning traffic. Also, all interactions between intersections are either assumed negligible (Assumption 4) or limiting for the entire airspace (Assumption 3). Hence, the mean number of instantaneous aircraft with resolution in the grid network can be obtained by summing $N_{i,WR}$ per leg l for the set of all legs L in the network:

$$\overline{N}_{i,WR,grid} = \sum_{l \in L} \overline{N}_{i,WR,l} = \sum_{l \in L} \left(\frac{D_l}{V_{NR}} + \overline{d}_l \right) \overline{q}_l \tag{23}$$

Additionally, following Assumption 1, the derived analytical delay model is assumed to act as an upper bound to experimental mean delay due to the overestimation of the time t_+ a crossing aircraft occupies an intersection. This overestimation is increased when more aircraft from the same origin leg cross without alternating with traffic from the crossing leg, i.e., for increasing density or flow ratio unbalance.

Lastly, an expression of the mean queue length (in meters) $\overline{L}$ can be used to approximate the stability limit of a given grid network airspace, as stated by Assumption 3. The mean queue length in a leg $\overline{L}_f$ can be calculated using Little's law (Little [18]) for the number of vehicles, multiplied by the horizontal separation requirement S_h:

$$\overline{L}_f = \overline{d}_f \overline{q}_f S_h \tag{24}$$

When $\overline{L}_f$ is greater than the distance to the next intersection, i.e., length of the leg D_f, the airspace becomes unstable.

5. Fast-time simulation design

In this section, the experimental setup is described. Multiple fast-time simulation experiments were performed to validate the analytical models and the assumptions as described in the previous sections. All experiments are performed using the BlueSky open-source ATM simulator (Hoekstra and Ellerbroek [12]). First, the tactical conflict detection and resolution algorithms are discussed, followed by a summary of the scenarios generated for the experiment. Finally, a model accuracy parameter is proposed, facilitating the comparison between the analytical model predictions and the experimental results.

5.1. Conflict detection and resolution

The state-based conflict detection algorithm used in this study is equal to the algorithm used by Sunil et al. [25] and assumes perfect knowledge of aircraft position and ground speed vector. In the algorithm, aircraft positions are linearly extrapolated along their ground speed vectors over a look-ahead time t_l of 20 seconds to predict intrusions.

Tactical conflict resolution is implemented, where each pairwise conflict is resolved using a speed-based resolution algorithm. This algorithm dictates that one aircraft decelerates to avoid the predicted intrusion. Recall from Equation (1) that the resolution speed V_{WR} is in the range $[0, V_{NR}\rangle$. For conflicts within an airway, the algorithm follows the International Rules of the Air (International Civil Aviation Organization [13]), dictating that an aircraft overtaking another aircraft needs to give way. For crossing conflicts, the aircraft which has to incur the slightest delay will perform the resolution. This aircraft is the aircraft that crosses on the rear-side of the other aircraft, i.e., the aircraft which, at the closest point of approach, has a relative bearing with the other aircraft in the range of $[-90°, 90°]$. During a simulation, both the detection and resolution algorithms are executed for each simulation timestep Δt of 0.05 seconds.

5.2. Scenario generation

A scenario generator was developed, which produces traffic scenarios at a desired, constant density. In contrast to Sunil et al. [26], aircraft are introduced at intervals following a random Poisson variable, i.e., exponentially distributed with a mean spawn rate $\overline{q}$. This departure rate is equivalent to the mean network flow rate $\overline{q}$ can be calculated by reversing Equation (5):

$$\overline{q} = \frac{V_{NR}}{\overline{D}} \overline{N}_{i,NR} \tag{25}$$

Furthermore, Table 1 summarises the common parameters are used in all simulations.

Table 1: Constant parameters used in the simulation experiments

Parameter	Value	Unit	Description
a	3.5	m/s^2	Acceleration or deceleration capability
D	200	m	Distance OD-node to intersection
S_h	50	m	Horizontal separation requirement
t_l	20	s	Look-ahead time
V_{NR}	10	m/s	Cruise speed of aircraft NR
V_{WR}	$[0, V_{NR}\rangle$	m/s	Possible range of speeds of aircraft WR (see Equation (1))
Δt	0.05	s	Simulation timestep
Repetitions	10	-	Number of repetitions per density for each experiment
Size	4x4	-	Number of flows (H x V)

For each experiment, scenarios for 10 densities with each 10 random initiations are generated. Three experiments are performed to show and validate the model's sensitivity to the independent variables V_{NR} and S_h. Firstly, a base experiment with the parameters outlined in Table 1 evaluates the accuracy of the analytical model. Secondly, a speed experiment with a cruise speed of 5m/s is used as a sensitivity analysis to validate and show the impact of changing V_{NR}. Thirdly, a horizontal separation requirement experiment is used with an S_h of 100 meters to validate and show the impact of changing S_h on the MFD. The base and speed experiment use 10 densities equally spaced from 6 to 60 $\overline{N}_{i,NR}$. As the separation experiment was unstable for densities larger than 25, the separation experiment uses 10 densities equally spaced from 2.5 to 25 $\overline{N}_{i,NR}$. The inputs of the experiments are summarised in Table 2. Altogether, 300 scenarios are generated for the experiments, involving more than 150 thousand aircraft in total.

In each scenario, all aircraft are assigned a departure time, origin, destination, and route. Each run uses a warming-up period of 15 minutes, a logging period of 45 minutes, and a cool-down period of 15 minutes in which aircraft keep spawning. The warming-up period ensures that the desired density and flow rates are reached before starting the logging period. The cool-down period ensures that aircraft in the logging period finish their trip at the desired airspace density, thereby preventing skewing of the

Table 2: Summary of experiment inputs

Experiment	Changed variable	$\overline{N}_{i,NR}$ range	Total no. of aircraft $['000]$
Base	-	$[6, 12, \ldots, 60]$	79
$0.5V_{NR}$	$V_{NR} \rightarrow 5$m/s	$[6, 12, \ldots, 60]$	40
$2S_h$	$S_h \rightarrow 100$m	$[2.5, 5, \ldots, 25]$	33

results. 15 minutes is deemed sufficient, as the maximum trip duration without resolution is less than 6 minutes in all experiments. Furthermore, when evaluating dependent airspace variables, such as the mean density or the mean delay, the values over the entire logging period are averaged.

The network environment consists of an orthogonal grid of two one-way airways in each direction, with the outer airways forming a counterclockwise flow, as depicted in Figures 5 and 6. Each aircraft is randomly assigned an origin (O) and a (different) destination (D) node from the set of OD-nodes. This set includes all nodes halfway between two intersections. To prevent instant intrusions between aircraft departing subsequently, the origin nodes of the three prior departures are excluded from the set of origin nodes for that aircraft. However, instant intrusions with cruising aircraft can still occur.

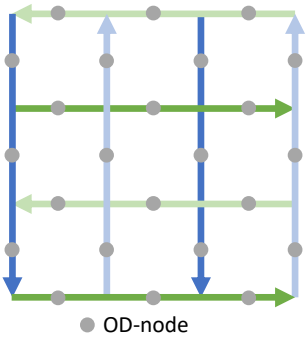

Figure 5: Orthogonal grid network structure

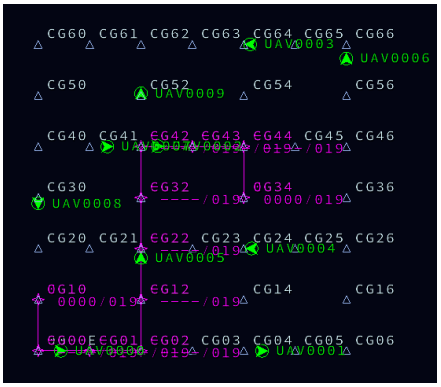

Figure 6: An example simulation run of the orthogonal grid network in BlueSky, with the path of UAV0000 shown in purple

The route is chosen based on the shortest path between the origin and destination node, taking into account the one-way restrictions. When multiple paths are equally short, the path with the least number of turns is chosen. As a result, only a single route is available for any OD combination.

5.3. Qualitatively and quantitatively estimating model accuracy

A qualitative assessment can be made of the accuracy by inspecting the similarity in shape and magnitude between the analytical model predictions and the experimental results. To also facilitate a quantitative comparison, the k-parameter is introduced (Sunil et al. [25]):

$$\text{Simulation measurement} = \text{Analytical model} \cdot k \tag{26}$$

This parameter is obtained by fitting the analytical model in a least-squares sense to the experimental data. A value close to 1 implies that the analytical model is accurate, whereas $k < 1$ and $k > 1$ imply an overestimation and an underestimation by the analytical model, respectively. In addition, to allow comparison of overestimation and underestimation k-parameters, the level of accuracy is expressed as a percentage by comparing k to a reference value of 1, using:

$$k_{\%} = \left(1 - \left|\frac{k-1}{k}\right|\right) \cdot 100\% \tag{27}$$

6. Results

In this section, the predictions of the analytical model are compared to the results of the three fast-time simulation experiments. With this comparison, the accuracy of the analytical model (derived in

Section 4) and the assumptions (made in Section 3) is assessed. This section concludes with the analytical model's prediction of the theoretical capacity limits of the three experimental set-ups.

6.1. Analytical model validation

In Figure 7, the comparison between the predictions of the analytical model and the results of the three fast-time simulation experiments is visualised. The three analytical model predictions are shown as solid lines, with the corresponding simulation experiment runs marked by an 'x' in the same colour. As can be seen, the analytical model closely predicts both the shape and the magnitude of the network flow rate. However, it slightly underestimates the experimental data for the higher densities.

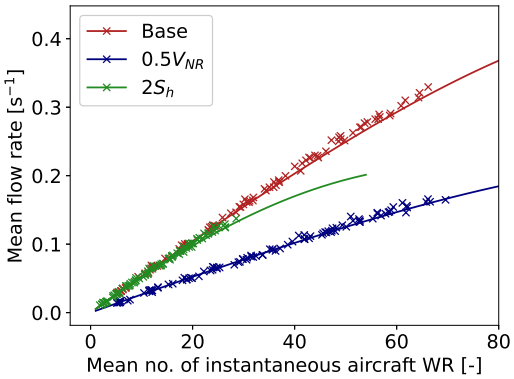

Figure 7: Comparison between the analytical model (solid line) and the fast-time simulation experiments (x) for the MFD for the three orthogonal grid network experiments. Note: respectively, 8, 1, and 9 experiment runs with the highest densities became unstable and are, therefore, not shown in the figure

In addition, the comparison between the analytical model and the three fast-time simulation experiments is expressed quantitatively in terms of k and $k_{\%}$ (as defined by Equations (26) and (27)) in Table 3. As expected, the values display $k > 1$, indicating an underestimation of the mean flow rate. However, as the mean flow rate is considered a known input variable, this underestimation is caused by the analytical model overestimating the mean density. Nevertheless, the accuracies of 97% and higher show that the model can closely predict the shape and magnitude of the network flow rate in a two-dimensional grid network airspace.

Table 3: Accuracy of the analytical model compared to the fast-time simulation experiments

Experiment	k	$k_{\%}$
Base	1.02	97.9%
$0.5V_{NR}$	1.02	97.8%
$2S_h$	1.03	97.4%

6.2. Theoretical capacities predicted by the analytical model

The analytical model allows the prediction of the theoretical maximum density and flow rate for an airspace with given parameters (e.g., cruise speed, size, separation distance), using Assumption 3 and Equation (24). The calculated values for the three experiments are shown in Table 4. The table shows that a change in cruise speed V_{NR} does not impact the maximum density. Furthermore, the network flow rate scales proportionally with the cruise speed. However, for a change in the horizontal separation requirement S_h, no proportionality is found. Increasing S_h means that both the maximum mean density and the maximum mean flow rate decrease.

Table 4: Theoretical capacities of the three experiments, shown as a combination of maximum stable density and stable flow rate

Experiment	Max. $\overline{N}_{i,WR}$ -	Max. $\overline{q}$ s^{-1}
Base	113	0.44
$0.5V_{NR}$	113	0.22
$2S_h$	58.1	0.21

7. Discussion

In this study, a purely analytical model for the relationship between the mean flow rate and the mean density, expressed in the Macroscopic Fundamental Diagram (MFD), was developed to investigate and quantify the factors influencing capacity of constrained urban airspace. Three fast-time simulation experiments were performed to validate the accuracy of the analytical model. In these experiments, over 150 thousand flights were simulated, flying in a small two-dimensional orthogonal grid network. This section discusses the level of accuracy of the analytical model, followed by a discussion on the effects of several airspace design parameters on capacity. It concludes by presenting further considerations and recommendations for future research.

7.1. Analytical model validation

The comparison of the analytical model with the results of three fast-time simulation experiments showed that model accuracy was high, with accuracies of more than 97%. The three fast-time experiments consisted of a base experiment and two sensitivity analyses, with one changing the cruise speed V_{NR} and one changing the horizontal separation requirement S_h, respectively. The analytical model closely predicted the shape and magnitude of the Macroscopic Fundamental Diagram. However, it overestimated the mean density by approximately 2% to 3% in all three experiments.

This slight overestimation can be explained by noting that, as mentioned in Section 4, the derived model acts as an upper bound on delay and, therefore, as an upper bound on the mean density. Namely, the model overestimates the time a crossing aircraft occupies an intersection when the upstream legs are not perfectly alternating. In the grid network airspace used in the experiments, the four busy intersections near the centre are unbalanced, having flow ratios between both upstream legs of approximately $1.7:1$. This imbalance explains the overestimation of the mean delay and the mean density.

Despite the limitation discussed above, the analytical model demonstrated the ability to estimate the Macroscopic Fundamental Diagram for a two-dimensional orthogonal grid network. Therefore, the derived model provides an effective tool to predict the effect of several airspace design parameters. In addition, the high level of accuracy validates utilisation of the theoretical maximum density defined by Assumption 3 to compare different constrained urban airspace designs, similar to the maximum density defined for general airspace by the CAMDA model (Sunil et al. [25]).

7.2. Effect of airspace design parameters

The level of accuracy of the analytical model allows for quantifying the effect of several relevant airspace design parameters. Based on the parameters used in the equations, three design parameters affect the capacity metrics used in this paper: the cruise speed V_{NR}, the horizontal separation requirement S_h, and the number of flow alternations at an intersection. The look-ahead time, when sufficiently long, does not affect the mean flow rate or the mean density. Additionally, the effect of the airspace structure, including, for example, the distance between intersections and the airspace area, is discussed.

When raising the cruise speed, aircraft can travel a longer distance in the same time window, increasing the mean network flow rate. Moreover, the mean delay per aircraft decreases as more aircraft can cross an intersection in the same time window. The analytical model predicts that the mean flow rate scales proportionally with the cruise speed V_{NR} when keeping the mean density constant. Furthermore, the maximum stable density defined by Assumption 3 remains unchanged. Hence, an increase in cruise speed is predicted to result in a proportional increase in the maximum flow rate and capacity.

For the horizontal separation requirement S_h, this proportionality is not present. Instead, the analyt-

ical model predicts that enlarging S_h reduces capacity. When S_h is increased, the maximum number of aircraft that fit within an airway is lowered, while the crossing times of aircraft are extended. Both factors increase the mean delay per aircraft, reducing the maximum flow rate and the maximum density.

Furthermore, capacity is predicted to be increased when the flows coming from the two upstream legs of an intersection alternate less frequently, as was stated in Assumption 1. Because the time window between two subsequent aircraft is increased by a factor $\sqrt{2}$ when the upstream flow is alternated (on an orthogonal intersection, see Equations (10) and (15)), capacity is decreased for each alternation. Therefore, a system limiting the number of alternations, for example, a traffic signal, may increase capacity. However, this system extends the mean queue length, increasing the chance of overflow. In this study, no exact model for an intersection with an alternation limiter is derived. Hence, the break-even point for the benefits of this system cannot be predicted. It is recommended to quantify this break-even point in further research.

Lastly, the structure of the airspace itself has a significant impact. When the distance between two neighbouring intersections is decreased, the probability of overflow increases, resulting in a reduced capacity. Contrarily, if this change results from an enlarged number of intersections and airways in the area, the capacity increases as the proportion of flyable airspace increases.

7.3. Further considerations

In this paper, a two-dimensional model is derived. However, a three-dimensional design is desired to utilise the available airspace fully. By substituting the vertical equivalents of the horizontal variables, e.g., the vertical separation requirement instead of S_h and the vertical speed instead of V_{NR}, the model is expected to be valid for a single vertical plane, two-dimensional airspace. If the airspace is subsequently modelled as the sum of intersections in either the vertical or the horizontal plane, an analytical model is obtained for a three-dimensional constrained urban airspace. Consider that model accuracy is expected to deteriorate when interactions between the vertical and horizontal intersections exist. The likelihood of these interactions increases when nodes are closer to each other. It is recommended to investigate the effect of these interactions in future research, to validate whether this model can be extended to the third dimension.

Furthermore, the derived model is validated for orthogonal intersections with up to two upstream legs only. In general, more complicated intersections exist with, for example, more than two upstream legs or non-orthogonal legs. It is hypothesised that the model can accurately predict the Macroscopic Fundamental Diagram at more complicated intersections, considering a few adjustments. Specifically, the red time r and the cycle time $\overline{c}_u$ need to be adjusted to include all crossing traffic and their respective crossing times. Further research is required to test this hypothesis.

Additionally, several limitations need to be considered for the findings in this paper. This study neglected meteorological effects, which may harm overall capacity. Nevertheless, the meteorological effects can be approximated using, e.g., an increased horizontal separation requirement S_h. Another limitation is the static demand assumed in both the analytical model and the fast-time simulation experiments. In reality, airspace demand changes from time to time in urban networks (Geroliminis and Daganzo [9]). Depending on the size of the airspace and rate of change of aircraft density, this may imply that during a ‘rush hour’, busy parts of the airspace can congest for a limited time without destabilising the entire airspace (in contrast to Assumption 3). When demand decreases at the end of the rush hour, the congestion gradually disappears. Note that the energy storage of drones is limited, making it plausible that congestion is to be prevented at all times.

8. Conclusion

The traffic density of small aerial vehicles within the highly constrained, low-altitude urban airspace is expected to increase significantly in the near future. An analytical approach is taken to increase understanding of the factors that influence the capacity of constrained urban airspace. The emergent behaviour of aircraft in constrained urban airspace, such as queueing and local hotspots, yields the existing analytical models for general airspace invalid. Therefore, in this paper, a new mathematical model is derived to estimate the relationship between the mean flow rate and the mean density, expressed in the Macroscopic Fundamental Diagram, for a two-dimensional orthogonal grid network. By performing three fast-time simulation experiments involving more than 150 thousand flights, the level of accuracy of the mathematical model is shown to be higher than 97%. This high level confirms the ability

of the model to closely predict the shape and magnitude of the Macroscopic Fundamental Diagram in the two-dimensional orthogonal grid network.

In addition, the high level of accuracy of the analytical model allows quantitative prediction of the effects of several relevant airspace design parameters on capacity. Notable findings showed that an increase in cruise speed leads to a proportional increase in the network flow rate while the maximum density is unaffected. Contrarily, enlarging the minimum separation distance reduces capacity. Additionally, turning traffic on balanced intersections does not impact the capacity more than through traffic. If routing with additional turns means that a shorter route is possible, efficiency may be increased. Lastly, a metric was defined describing a theoretical maximum density, which can rank different constrained urban airspace designs on capacity.

Furthermore, in a stable environment, the model predicts that the constrained urban airspace can destabilise when the maximum capacity of a single intersection only is reached. Additionally, for intersections operating at near-maximum capacity, measures limiting flow alternation, such as traffic signals, potentially improve the efficiency of an intersection of airways.

All in all, the results demonstrate how the derived analytical model for the Macroscopic Fundamental Diagram provides an increased understanding of the factors that influence the capacity of constrained urban airspace, thereby offering an effective tool for urban airspace design applications. Furthermore, this model lays the groundwork for the derivation of more expanded models, including the altitude dimension and non-orthogonal or non-four-way intersections, enabling an increased understanding of the constrained urban airspace.

Acknowledgements

The author would like to thank Joost Ellerbroek and Victor Knoop for their continuous advice and coaching throughout this MSc. thesis. The lively discussions over the (dis)similarities between road transportation and urban traffic management research were essential for the insights, results, and conclusions presented in this paper. Furthermore, the community behind the BlueSky open-source ATM simulator project made it possible to set up and perform multiple fast-time simulation experiments with high fidelity in just a few weeks, which was essential in making the deadline. Additionally, the valuable input of Jacco Hoekstra was very welcome. Lastly, the author would like to thank his family and friends, who kept him happy, healthy, and motivated throughout his entire studies at the TU Delft.

Bibliography

[1] Karl D. Bilimoria, Kapil S. Sheth, Hilda Q. Lee, and Shon R. Grabbe. Performance evaluation of airborne separation assurance for free flight. In *18th Applied Aerodynamics Conference*, 2000. doi: 10.2514/atcq.11.2.85.

[2] Carlos F. Daganzo, Vikash V. Gayah, and Eric J. Gonzales. Macroscopic relations of urban traffic variables: Bifurcations, multivaluedness and instability. *Transportation Research Part B: Methodological*, 45(1):278–288, 1 2011. ISSN 01912615. doi: 10.1016/j.trb.2010.06.006.

[3] K. Datta and R. M. Oliver. Predicting risk of near midair collisions in controlled airspace. *Transportation Research Part B*, 25(4), 1991. ISSN 01912615. doi: 10.1016/0191-2615(91)90006-5.

[4] Malik Doole, Joost Ellerbroek, and Jacco Hoekstra. Estimation of traffic density from drone-based delivery in very low level urban airspace. *Journal of Air Transport Management*, 88, 9 2020. ISSN 09696997. doi: 10.1016/j.jairtraman.2020.101862.

[5] Malik Doole, Joost Ellerbroek, Victor L. Knoop, and Jacco M. Hoekstra. Constrained Urban Airspace Design for Large-Scale Drone-Based Delivery Traffic. *Aerospace*, 8(2):38, 2 2021. ISSN 2226-4310. doi: 10.3390/aerospace8020038.

[6] Shinsuke Endoh. Aircraft Collision Models. Technical report, Massachusetts Institute of Technology, Cambridge, Massachusetts, USA, 1982. URL http://dspace.mit.edu/handle/1721.1/68072.

[7] Federal Aviation Administration. Overview of Small UAS Notice of Proposed Rulemaking. United States Department of Transportation. Notice No. 15-01, 2015.

[8] Vikash V. Gayah and Carlos F. Daganzo. Clockwise hysteresis loops in the Macroscopic Fundamental Diagram: An effect of network instability. *Transportation Research Part B: Methodological*, 45(4):643–655, 5 2011. ISSN 01912615. doi: 10.1016/j.trb.2010.11.006.

[9] Nikolas Geroliminis and Carlos F. Daganzo. Existence of urban-scale macroscopic fundamental diagrams: Some experimental findings. *Transportation Research Part B: Methodological*, 42(9): 759–770, 11 2008. ISSN 01912615. doi: 10.1016/j.trb.2008.02.002.

[10] Walton Graham and Robert H Orr. Terminal Air Traffic Flow and Collision Exposure. In *Proceedings of the IEEE*, pages 328–336. IEEE, 3 1970. doi: 10.1109/PROC.1970.7638.

[11] J. M. Hoekstra, R. C. J. Ruigrok, and R. N. H. W. van Gent. Free Flight in a Crowded Airspace? In *Proceedings of the 3rd USA/Europe Air Traffic Management R&D Seminar*, Napoli, 2000.

[12] Jacco M. Hoekstra and Joost Ellerbroek. BlueSky ATC simulator project: an open-data and open-source approach. In *Proceedings of the 7th International Conference on Research in Air Transportation*, Philadelphia, USA, 2016.

[13] International Civil Aviation Organization. *Rules of the Air - Annex 2*. 10th edition, 2005. ISBN 2373438925.

[14] Dae Sung Jang, Corey Ippolito, Shankar Sankararaman, and Vahram Stepanyan. Concepts of airspace structures and system analysis for UAS traffic flows for urban areas. In *AIAA Information Systems-AIAA Infotech at Aerospace, 2017*. American Institute of Aeronautics and Astronautics Inc, AIAA, 2017. ISBN 9781624104497. doi: 10.2514/6.2017-0449.

[15] Matt R. Jardin. Analytical relationships between conflict counts and air-traffic density. *Journal of Guidance, Control, and Dynamics*, 28(6):1150–1156, 2005. ISSN 15333884. doi: 10.2514/1.12758.

[16] V. Knoop, S. Hoogendoorn, and J. Van Lint. Routing strategies based on macroscopic fundamental diagram. *Transportation Research Record*, (2315):1–10, 12 2012. ISSN 03611981. doi: 10.3141/2315-01.

[17] James K. Kuchar and Lee C. Yang. A Review of Conflict Detection and Resolution Modeling Methods. *IEEE Transactions on Intelligent Transportation Systems*, 1(4):179–189, 12 2000. ISSN 15249050. doi: 10.1109/6979.898217.

[18] John D. C. Little. A Proof for the Queuing Formula: L = λ W. *Operations Research*, 9(3): 383–387, 6 1961. ISSN 0030-364X. doi: 10.1287/opre.9.3.383.

[19] Niklas Peinecke and Alexander Kuenz. Deconflicting the urban drone airspace. In *AIAA/IEEE Digital Avionics Systems Conference - Proceedings*, volume 2017-September, 2017. doi: 10.1109/DASC.2017.8102048.

[20] Marta Ribeiro, Joost Ellerbroek, and Jacco Hoekstra. Velocity obstacle based conflict avoidance in urban environment with variable speed limit. *Aerospace*, 8(4):93, 4 2021. ISSN 22264310. doi: 10.3390/aerospace8040093. URL https://doi.org/10.3390/aerospace8040093.

[21] Mohamed Faisal Bin Mohamed Salleh, Da Yang Tan, Choon Hian Koh, and K. H. Low. Preliminary concept of operations (ConOps) for traffic management of unmanned aircraft systems (TM-UAS) in urban environment. In *AIAA Information Systems-AIAA Infotech at Aerospace, 2017*, 2017. doi: 10.2514/6.2017-0223.

[22] Mohammed Faisal Bin Mohammed Salleh, Wanchao Chi, Zhenkun Wang, Shuangyao Huang, Da Yang Tan, Tingting Huang, and K. H. Low. Preliminary concept of adaptive urban airspace management for unmanned aircraft operations. In *AIAA Information Systems-AIAA Infotech at Aerospace, 2018*, 2018. doi: 10.2514/6.2018-2260.

[23] Emmanuel Sunil, Jacco Hoekstra, Joost Ellerbroek, Frank Bussink, Dennis Nieuwenhuisen, Andrija Vidosavljevic, and Stefan Kern. Metropolis: Relating airspace structure and capacity for extreme traffic densities. In *Proceedings of the 11th USA/Europe Air Traffic Management Research and Development Seminar, ATM 2015*, 2015.

[24] Emmanuel Sunil, Joost Ellerbroek, Jacco Hoekstra, Andrija Vidosavljevic, Michael Arntzen, Frank Bussink, and Dennis Nieuwenhuisen. Analysis of airspace structure and capacity for decentralized separation using fast-time simulations. *Journal of Guidance, Control, and Dynamics*, 40(1):38–51, 2017. ISSN 15333884. doi: 10.2514/1.G000528.

[25] Emmanuel Sunil, Joost Ellerbroek, and Jacco Hoekstra. CAMDA: Capacity Assessment Method for Decentralized Air Traffic Control. In *2018 International Conference on Research in Air Transportation: Barcelona, Spain, 2018*. APA, 2018. URL http://resolver.tudelft.nl/uuid:4bfdfe42-3948-4e98-9997-501f2056e3bf.

[26] Emmanuel Sunil, Joost Ellerbroek, Jacco M. Hoekstra, and Jerom Maas. Three-dimensional conflict count models for unstructured and layered airspace designs. *Transportation Research Part C: Emerging Technologies*, 95:295–319, 10 2018. ISSN 0968090X. doi: 10.1016/j.trc.2018.05.031.

[27] Emmanuel Sunil, Olafur Þórðarson, Joost Ellerbroek, and Jacco Hoekstra. Analyzing the Effect of Traffic Scenario Properties on Conflict Count Models. In *2018 International Conference on Research in Air Transportation: Barcelona, Spain, 2018*, 2018. URL http://resolver.tudelft.nl/uuid:4259c280-bd4c-4ace-8c42-413aa8aba6d3.

[28] Gabriel Tilg, Sasan Amini, and Fritz Busch. Evaluation of analytical approximation methods for the macroscopic fundamental diagram. *Transportation Research Part C: Emerging Technologies*, 114:1–19, 5 2020. ISSN 0968090X. doi: 10.1016/j.trc.2020.02.003.

[29] F. V. Webster. Traffic signal settings. *Road Research Technical Paper, No.39, Road Research Laboratory, London*, 1958.

Appendices

The appendices start with a nomenclature of the symbols used in the paper in Appendix A. Subsequently, in Appendix B, a set-up of fast-time simulation experiments for a single intersection environment is presented. Four experiments were performed on this single intersection environment to inspect further the assumptions made in Section 3 regarding, for example, turning traffic. First, a comparison is included between the analytical model predictions and the experiment results for the mean delay and the mean flow rate. Next, various considerations regarding the behaviour of the analytical model at the border intersections in the grid network are made in Appendix C.

Appendix D expands on the working of the fast-time simulation experiments. Appendix D.1 elaborates on the conflict resolution algorithms and includes a short validation of their capability of preventing intrusions in the experiments. Subsequently, Appendix D.2 explains the effects of airspace instability in the grid network environment in BlueSky. Lastly, Appendix D.3 shows the mean flow rates per grid network leg.

Next, additional analytical models are presented in Appendices E and F. Firstly, Appendix E shows the derivation and validation of two analytical conflict count models for constrained urban airspace, i.e., one without and one with conflict resolution. The Domino Effect Parameter is discussed as well. Secondly, Appendix F presents various other derivations, such as an intrusion count model. In the same appendix, these models are compared to the fast-time simulation experiment results to validate their accuracy.

Lastly, Appendix G includes miscellaneous results of the comparisons between the fast-time simulation experiments and the analytical models not yet included in the rest of the paper.

A. Nomenclature

In this appendix, the nomenclature used in this paper is summarised. Table 5 includes the Greek letter symbols, while Table 6 displays the Roman letter symbols. The subscripts and superscripts are stated in Table 7, whereas the abbreviations are gathered in Table 8. Additional symbols and abbreviations used in the appendices are not included.

Table 5: Nomenclature: Greek letters

Parameter	Unit	Description
Δ	-	Difference
λ	-	Green time proportion
ψ	rad	Ground track angle

Table 6: Nomenclature: Roman letters

Parameter	Unit	Description
A	m^2	Area
D	m, or -	Flight distance, or set of downstream legs d
F	-	Set of legs f, union of sets U and D
I	-	Set of all intersection nodes n in the grid network
L	m	Queue length, or set of all legs l in a network
N	-	Number of aircraft
S_h	m	Horizontal separation minimum
S	m	Separation distance
U	-	Set of upstream legs u
V	m/s	Airspeed
a	m/s^2	Acceleration of deceleration capability
c	s	Cycle time (sum of red and green signal times)
d	s, -	Delay, or downstream leg of an intersection
f	-	Leg of an intersection
k	-	Model accuracy
l	-	Leg in a network
q	s^{-1}	Flow rate
s	s^{-1}	Maximum / saturation flow rate
t	s	Time / duration
u	-	Upstream leg of an intersection
x	-	Degree of saturation (of an upstream flow)

Table 7: Nomenclature: sub- and superscripts

Script	Description
$_{NR}$	No conflict resolution
$_{R}$	Reaction
$_{WR}$	With conflict resolution
$_{c}$	of the crossing flow (rate)
$_{f}$	Of an intersection leg
$_{g}$	General
$_{i}$	Instantaneous
$_{l}$	Look-ahead (time), or of a leg in the network
$_{los}$	Intrusion (loss of separation)
$_{s}$	Stochastic
$_{u}$	Of an upstream leg
$_{\angle}$	Including corner / over the path
$_{+}$	Between crossing flows (on the intersection), or entire intersection flow rate
$_{\parallel}$	Within an airway
$_{\%}$	In percentage
–	Mean of

Table 8: Nomenclature: abbreviations

Abbreviation	Description
ATM	Air traffic management
CPA	Closest point of approach
DEP	Domino effect parameter
E	Eastbound
EN	East- to northbound turn
MFD	Macroscopic Fundamental Diagram
N	Northbound
NE	North- to eastbound turn
NR	No conflict resolution
PAV	Personal aerial vehicle
UAV	Unmanned aerial vehicle
WR	With conflict resolution

B. Single intersection validation experiments

Next to the three grid network experiments outlined in Section 5, four experiments were performed for a single intersection simulation environment. These experiments are used to analyse aircraft interactions and the effect of turning traffic in more detail. This appendix presents the set-up of the four fast-time simulation experiments and, subsequently, shows the results and a discussion of the comparison between the analytical delay model of Section 4 and the experiments.

B.1. Fast-time simulation experiment design for the single intersection environment

The single intersection environment is equivalent to the intersection of Figure 4, with two possible origins (west and south) and two possible destinations (east and north). Each leg of the intersection has a length of 1km. Different scenarios are generated to compare the behaviour of the analytical model over a range of densities. Therefore, the mean intersection flow rate $\overline{q}_+$ is uniformly varied 10 times between $0.05s_+$ and $0.95s_+$, where s_+ represents the intersection crossing capacity defined by Equation (11). After the generation of the departure times, pre-departure separation is applied on the aircraft of the two flows in each upstream leg (i.e., one straight and one turning flow) to prevent instant intrusions.

Three different flow ratios with directions (E/N/EN/NE) are used for the experiment. As a base experiment, an intersection with flow ratio $(0.6/0.4/0/0)$, i.e., without turning traffic, is chosen. A second experiment is included with a flow ratio of $(0.8/0.2/0/0)$ to assess the accuracy of the analytical model for less balanced intersections. The third experiment equals the base experiment with 10% turning traffic, meaning a flow ratio of $(0.54/0.36/0.06/0.04)$. This experiment is used to validate the assumptions regarding turning traffic. All in all, 300 scenarios are generated for these three experiments.

A fourth experiment is performed to validate the turning traffic assumptions even further. In this experiment, the same $\overline{q}_+$ equal to $0.7s_+$ is used for each run, using the flow ratio of the base experiment $(0.6/0.4/0/0)$. The percentage of turning traffic is varied 10 times uniformly from 5% to 95%. Hence, 10 flow ratios ranging from $(0.57/0.38/0.03/0.02)$ to $(0.03/0.02/0.57/0.38)$ are simulated, each with 10 repetitions. All intersection experiments are summarised in Table 9.

Table 9: Intersection simulation experiments summary

Flow ratio (E/N/EN/NE)	Mean departure rate [veh/s]	No. of runs [-]	No. of aircraft ['000]
$(0.6/0.4/0/0)$	$[0.007, \dots, 0.133]$	100	31
$(0.8/0.2/0/0)$	$[0.007, \dots, 0.133]$	100	31
$(0.54/0.36/0.06/0.04)$	$[0.007, \dots, 0.133]$	100	31
$[(0.57/0.38/0.03/0.02), \dots, (0.03/0.02/0.57/0.38)]$	0.098	100	44

B.2. Single intersection environment results and discussion

Figure 8 and Table 10 show the comparison between the analytical model and show the simulation experiments for the mean intersection delay. The model for $(0.54/0.36/0.06/0.04)$ is not visible, as it is equal to the $(0.6/0.4/0/0)$ model. For low to medium densities, the model of Equation (21) closely approximates the experimental data. For higher densities, the analytical model underestimates the observed delay for $(0.6/0.4/0/0)$ and $(0.54/0.36/0.06/0.04)$, whereas the model for $(0.8/0.2/0/0)$ shows an overestimation. The values for k reflect this over- and underestimation as well. The overestimation of the $(0.8/0.2/0/0)$ experiment signifies the validity of Assumption 1, as the upstream leg is alternating less often compared to the other experiments. At the same time, the underestimation of the delay for the more balanced simulations can be explained by the variation over time of the aircraft density. As the analytical delay model does not scale linearly with the mean density, an analytical prediction using the mean density will underestimate the mean delay. Moreover, the stochastic part of the analytical delay model has a quadratic relation with density (see Equation (19)), resulting in a more substantial underestimation for higher densities.

Next to the delay, the Macroscopic Fundamental Diagram in the mean flow rate versus the mean density is shown in Figure 9 and Table 10. As this is directly linked to the mean delay plot, the analysis made for the mean delay comparison holds.

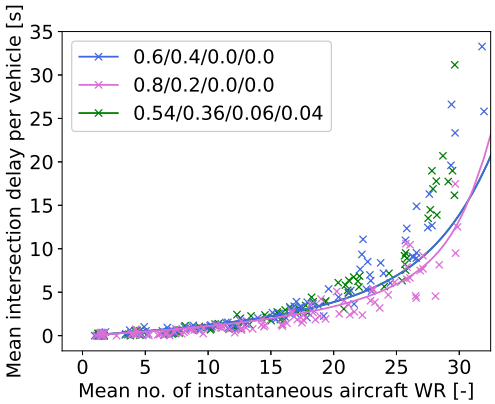

Figure 8: Comparison between the analytical model (solid line) and the fast-time simulation experiment (x) for $\overline{d}$ on the intersection (the analytical model for the $(0.54/0.36/0.06/0.04)$ experiment overlaps with the model for the $(0.6/0.4/0/0)$ experiment and is not visible)

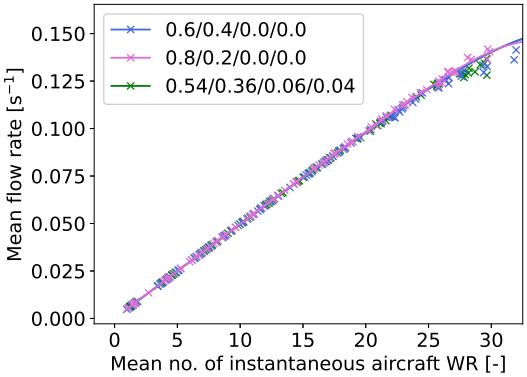

Figure 9: Comparison between the analytical model (solid line) and the fast-time simulation experiment (x) for the mean flow rate of the intersection experiments

Table 10: Accuracy of the model for the mean delay and the mean flow rate on the intersection

	Mean delay [s]		Mean flow rate [s^{-1}]	
Flow ratio	k	$k_{\%}$	k	$k_{\%}$
$(0.6/0.4/0/0)$	1.60	62.5%	0.986	98.6%
$(0.8/0.2/0/0)$	0.912	90.4%	0.987	98.7%
$(0.54/0.36/0.06/0.04)$	1.53	65.4%	1.00	99.8%
Turn experiment	0.980	98.0%	1.00	99.9%

Assumption 2 states that turning traffic has an equal impact on delay as non-turning traffic. This assumption is validated in Figures 10 and 11. Per Table 10, the accuracy difference in mean delay is 2% in terms of $k_{\%}$, similar to the value seen for the base ratio $(0.6/0.4/0/0)$ around that density in Figure 8. Furthermore, when fitting a first-degree polynomial (i.e., $ax + b$) to the experimental data, the rate of change in delay (a) per ratio of turning traffic (x) equals $-1.26 \cdot 10^{-4}$. Hence, when all aircraft are turning, the delay is decreased by approximately one per cent compared to the case when all aircraft head straight. Therefore, Assumption 2 is deemed valid.

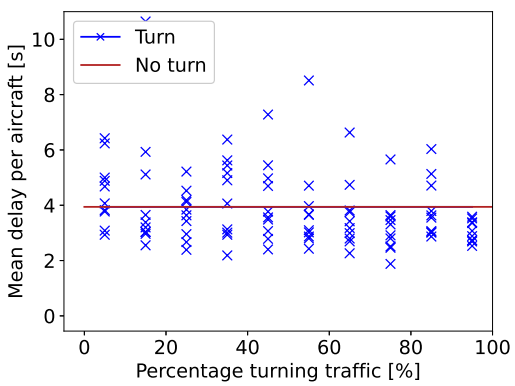

Figure 10: Comparison between the analytical model (solid line) and the fast-time simulation experiment (x) for the mean delay $\overline{d}$ per turn percentage with as base flow ratio (0.6/0.4/0/0) and $\overline{q}_+ = 0.7s_+$

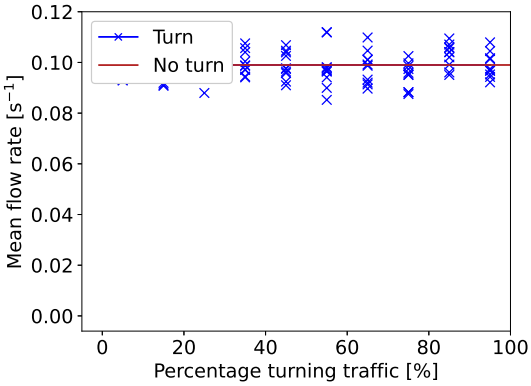

Figure 11: Comparison between the analytical conflict count model (solid line) and the fast-time simulation experiment (x) for mean flow rate per turn percentage with as base flow ratio $(0.6/0.4/0/0)$ and $q_+ = 0.7s_+$

C. Modelling border intersections and departures in the grid network

Border intersections and departure nodes in the orthogonal grid network environment form particular cases of orthogonal intersections. The impact of these intersections on the accuracy of the analytical model of Section 4 is discussed in this appendix. Three types of border intersections are considered: a T-intersection with one upstream leg, shown in Figure 12, a T-intersection with two upstream legs, shown in Figure 13, and a corner intersection, shown in Figure 14. Departure nodes are considered a specific case of a T-intersection with two upstream legs. All analyses presented are valid for the turned and mirrored versions of these intersections as well.

For the T-intersection with one upstream leg, only case 1 (recall Section 3) turning traffic is present. In other words, each aircraft turns and conflicts occur for each aircraft that is following within a distance of S_+ (defined by Equation (4)). As a result, an increase in delay occurs, which is not compensated for by an equivalent decrease in delay incurred by traffic coming from the other upstream arm. Therefore, at such intersections, Assumption 2 is deemed invalid. However, no specific model has been derived for these cases. Instead, the analytical model is calculated as if Assumption 2 would be valid, and aircraft at these intersections are modelled to experience no delay. It is recommended to investigate the delay at such three-way intersections in future research.

For the T-intersection with two upstream legs, the flow ratio is given by $(0/x/y/0)$, with the sum of x and y being 1. In this case, two upstream legs exist, which generate crossing conflicts and delay. The difference with the regular model is that one of the upstream legs does not continue downstream. Similar to the T-intersection with one upstream leg, the turning aircraft provoke a conflict for each aircraft in its airway trailing within a distance of S_+. However, contrary to the T-intersection with one upstream leg, the turn performed by aircraft coming from the west in Figure 13 lowers the delay of aircraft coming from the south compared to when the turning aircraft would have headed straight. Therefore, Assumption 2 is deemed valid at these intersections, and the model can be used as if the intersection is a regular four-way orthogonal intersection.

The corner intersection is a particular case of the T-intersection with one upstream leg, with the percentage turning traffic at 100%. Similar to the T-intersection with one upstream leg, only an increase in delay is present. Again, these intersections are modelled to experience no delay.

Next to regular four-way intersections and the above described three-way and corner intersections, departure traffic is present in the orthogonal grid network airspace. A departure node in the network is comparable to a T-intersection with two upstream legs, with the length D_f of the upstream departure leg being infinitesimally small. As $D_f \approx 0$, by Equation (5), the number of instantaneous aircraft without resolution $N_{i,NR}$ equals zero. In Figure 13, the turning leg (coming from the west) is replaced by this infinitesimally small leg. Note that departing traffic heads directly in the northbound direction and does not turn. In addition, it instantly flies at cruise speed. Hence, no conflicts occur with other cruising aircraft unless downstream traffic has decelerated for a different conflict. However, departing traffic

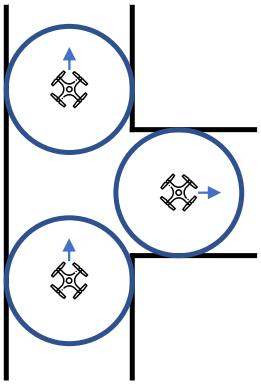

Figure 12: Border T-intersection, with one upstream leg and two downstream legs and flow ratio $(0/x/0/y)$ $(x + y = 1)$

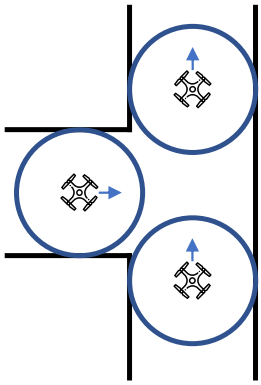

Figure 13: Border T-intersection, with two upstream legs and one downstream leg and flow ratio $(0/x/y/0)$ $(x + y = 1)$

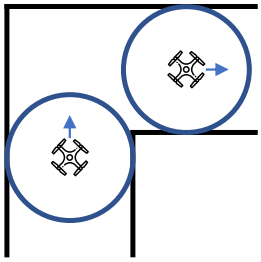

Figure 14: Corner intersection, with one upstream leg and one downstream leg and flow ratio $(0/0/0/1)$

does generate a delay when instant intrusions occur. The delay for departing traffic is incurred in the infinitesimally small upstream leg, increasing the number of instantaneous aircraft WR $N_{i,WR}$ in that leg by Equation (7). Because the departing traffic heads in the same direction as the cruising traffic, r equals $S_{\parallel}/V_{NR}$, as the angle between both ground tracks $\Delta\psi = 0$ rad (see Equations (2) and (10)). The latter needs to be taken into account in the calculation of the general delay by Equation (18).

D. Two-dimensional orthogonal grid network experiment design

This appendix expands on the working of the fast-time simulation experiments, allowing verification and repetition of the simulations. As mentioned in Section 5, the simulation platform used is BlueSky (Hoekstra and Ellerbroek [12]). The Python code developed for the simulation experiments is open-source and can be found at `https://github.com/michielaarts/bluesky`. This appendix first elaborates on the speed-based conflict resolution algorithms for crossing conflicts and within airway conflicts. Next, several remarks on instability in the orthogonal grid network airspace in BlueSky are made. Finally, the flow rate proportions are presented, substantiating the statement made in Section 7 of an upstream flow imbalance of $1.7:1$ for the four centre intersections.

D.1. Speed-based conflict resolution algorithms

In this section, the exact speed-based conflict resolution algorithms used in the fast-time simulation experiments are discussed. Each pairwise conflict is resolved using a tactical speed-based resolution algorithm, with one aircraft decelerating to avoid the intrusion. Recall from Equation (1) that the resolution speed V_{WR} is in the range $[0, V_{NR}\rangle$.

In a 2D constrained airspace, two conflict types can be distinguished: crossing conflicts and within airway conflicts. In the simulation, a within airway conflict is defined as a conflict in which the angular difference between the aircraft's ground tracks is less than $10°$. All other conflicts are crossing conflicts. Consider that, as conflicts are solved speed-based only, head-on conflicts within an airway are not resolvable. Therefore, two-way airways are not feasible with this algorithm.

The entire resolution algorithm, including all resolution speeds V_{WR}, is (re)calculated for each conflict (and intrusion) each simulation timestep Δt of 0.05 seconds. This recalculation allows for corrections during the resolution. Corrections are needed when, for example, the leading aircraft decelerates for a different conflict. The calculated V_{WR} acts as a target speed. Depending on the acceleration capabilities of the aircraft, it may reach its target speed earlier or later. Nevertheless, as the target speed is continuously updated, the final delay incurred will be equal (i.e., resolving the conflict by avoiding the intrusion with the least distance possible). When an aircraft is in multiple conflicts simultaneously, the lowest V_{WR} will be set as the target.

This section first presents the definition of the algorithms of the crossing conflicts and the within airway conflicts, respectively. Subsequently, a small validation is included to confirm the ability of the conflict resolution algorithms to prevent intrusions.

D.1.1. Resolution of crossing conflicts

Consider the two aircraft in a crossing conflict depicted in Figure 15. In the illustrated situation, the closest point of approach (CPA) lies behind aircraft A. Hence, aircraft B has to give right-of-way and incur at least delay d to completely resolve the crossing conflict. d can geometrically be derived to be:

$$d = \frac{dist(CPA_{NR} \rightarrow CPA_{WR})}{V_B \sin \angle(V_{r,NR}, V_B)} \tag{28}$$

Due to aircraft B decelerating to resolve the conflict, a second crossing aircraft might be predicted to cross in front based on the current velocity vectors. This behaviour is undesirable, as the first-come, first-serve property of the intersection is violated. Therefore, detecting whether the CPA lies in front or behind an aircraft is performed using the cruise velocities instead of the actual WR velocities.

Aircraft efficiency is higher when accelerations and decelerations are limited. Therefore, to resolve the conflict as efficiently as possible, aircraft B has to start decelerating to resolution speed $V_{+,WR}$ directly upon detection and incur the delay in the time remaining to the intrusion t_{los}:

$$V_{+,WR} = V_{NR} \cdot \frac{t_{los}}{d + t_{los}} \tag{29}$$

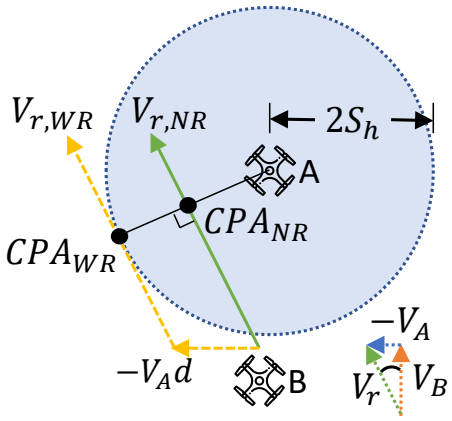

Figure 15: A crossing conflict, as seen from the relative frame of aircraft A. B has to incur at least delay d to follow the resolution vector, shown in dashed yellow, and ensure the closest point of approach with resolution CPA_{WR} remains outside the protected zone.

Recall that V_{WR} is recalculated for each simulation timestep. Hence, the acceleration rate does not impact the final incurred delay, only the profile of the resolution speed.

D.1.2. Resolution of within airway conflicts

In Figure 16, the leading aircraft A flies slower than the following aircraft B. To prevent an intrusion, aircraft B must slow down to ensure that the CPA remains outside the protected zone around A. In contrast to the crossing conflict, it is not beneficial for B to decelerate immediately. When B would slow down instantly, a gap would remain between B and A, reducing capacity within an airway or at intersections. Instead, B wants to approach as closely as possible while still preventing an intrusion. Assuming equal decelerating capabilities of all aircraft in the airspace, this can be modelled as a reaction time t_R at which B keeps t_{los}. In this paper, the reaction time t_R equals 5 seconds. The resulting within airway resolution speed $V_{\parallel,WR}$ for the following aircraft is defined by:

$$V_{\parallel,WR} = \begin{cases} V_{NR} & t_{los} \geq t_R \\ V_{NR} \cdot \frac{t_{los}}{t_R} & t_{los} < t_R \end{cases} \tag{30}$$

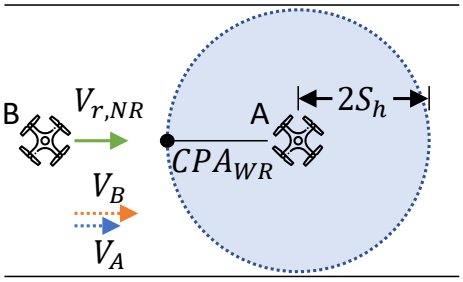

Figure 16: A within airway conflict, as seen from the relative frame of aircraft A. B has to keep incurring delay to ensure the closest point of approach with resolution CPA_{WR} remains outside the protected zone.

Again, V_{WR} is recalculated for each simulation timestep. Therefore, V_{WR} keeps on converging to the speed of the leading aircraft. As V_{WR} acts as a target, the actual resolution speed profile depends on the acceleration rate.

D.1.3. Conflict resolution algorithm validation

The goal of the speed-based resolution algorithm is to prevent all intrusions. However, several effects are present which hamper the performance of the algorithm. To inspect if the speed-based conflict

resolution algorithm works as desired, Figure 17 and Figure 18 show the total number of intrusions for the intersection (see Appendix B.1) and the grid network experiments (see Section 5), respectively.

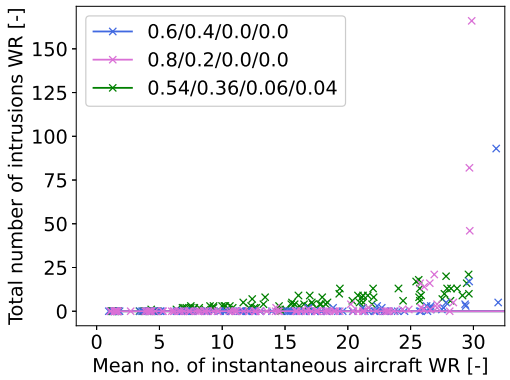

Figure 17: Total number of intrusions for the intersection experiments

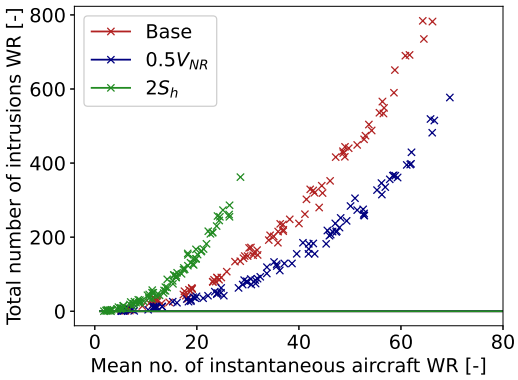

Figure 18: Total number of intrusions for the grid network experiment

At low to medium densities, all conflicts are resolved before an intrusion occurs for the intersection experiments without turning traffic (experiments $(0.6/0.4/0/0)$ and $(0.8/0.2/0/0)$). At densities close to saturation, Assumption 3 predicts that overflow may occur, leading to airspace instability. The model indicates that the maximum capacity defined by Assumption 3 is reached at a density of approximately $30N_{i,WR}$. The outliers present in Figure 17 confirm this assumption at densities higher than 30. In these simulation runs, the queue extended to the departure locations of the aircraft. As a result, departing aircraft are in an intrusion instantly upon departure, which the algorithm cannot prevent.

With turning traffic (experiment $(0.54/0.36/0.06/0.04)$), the number of intrusions increases with increasing density. Visual inspection of these conflicts in BlueSky showed that these intrusions are caused by short-term, turning out-of-airway conflicts (see Section 3.2). In such conflicts, the time window between detection and the intrusion is too tiny, thereby not allowing the closely trailing aircraft to prevent the intrusion within its acceleration capabilities. However, aircraft in an intrusion still try to evade this intrusion. Upon exiting the intrusion, the amount of delay incurred by the trailing aircraft is approximately equal to the amount of delay in an environment with instant deceleration. Therefore, the conflict resolution algorithm works as desired for the intersection experiments.

For the grid network experiment, shown in Figure 18, a similar increase in the total number of intrusions with increasing density is seen. On top of the intrusions due to turning traffic, as found in the intersection experiment, departing aircraft may instantly spawn in an intrusion. These intrusions are not prevented, as no departure separation nor climbing to cruise altitude is used in the experiment. Upon detecting such an intrusion, it is resolved as a conflict by incurring delay using Equation (30). The combination of the instant departure intrusions and the turning out-of-airway intrusions explains the increase. Therefore, it is concluded that the conflict resolution algorithm also works as desired for the orthogonal grid network experiment.

D.2. Remarks on airspace instability in the grid network environment

Assumption 3 predicts that the airspace destabilises once a single queue extends to an upstream node. Recall Figure 3, which illustrated this instability. This appendix explains how instability emerges in the BlueSky simulation platform and offers (partial) solutions to avoid this instability.

In the BlueSky simulation environment, unstable airspace is encountered as well, see Figure 19. In this figure, the centre block of the grid network is shown, experiencing overflow in a run with a desired mean density of $\overline{N}_{i,NR} = 100$. All aircraft are standing still ($V_{WR} = 0$). This gridlock can be understood starting from aircraft UAV0038 at the top-left intersection. UAV0038 is blocked by the overflow occurring in the eastbound airway between nodes CG42 and CG44. In itself, UAV0038 obstructs the northbound traffic upstream of UAV0038. The longer the duration of such a stoppage, the longer the queue in the northbound airway between CG22 and CG42 becomes. At the instant of Figure 19, the line extends to the upstream intersection CG22 in the bottom left corner. As a result, the westbound airway at the bottom is blocked and, in turn, blocking the southbound airway, blocking the eastbound airway, etc.

Figure 19: A BlueSky screenshot of a city block experiencing overflow in the orthogonal grid network simulation. The arrows signify other legs of the network. Aircraft UAV0038 at the top left intersection is blocked by overflow occurring in the eastbound airway at the top. As a result, a queue started to form, extending all the way upstream to intersection CG22 in the bottom left, blocking the flows there as well

The stranded aircraft around the city block of Figure 19 cannot reach their destination anymore, while new aircraft keep spawning. Hence, if this simulation is allowed to continue, density keeps increasing, more airways get saturated, and the entire network converges to a complete standstill. When the simulation run finishes, these aircraft have not reached their destinations. Hence, neither the flight times, nor the mean velocities, nor the mean delays can be extracted from the simulation experiment. Therefore, simulations with an unstable flow do not provide usable results with the current simulation setup.

A prerequisite for the manifestation of unstable environments is the zero minimum airspeed setting, as defined by Equation (1). If the minimum airspeed is set at a higher level (e.g., Doole et al. [5], Ribeiro et al. [20]), airspace operating above its capacity limits will result in the emergence of intrusions instead of instability. Namely, aircraft cannot decelerate sufficiently to resolve the conflicts and avoid the intrusions. Additionally, this minimum airspeed setting is expected to be a major factor for the difference in simulated behaviour between Doole et al. [5] and this paper (discussed in Appendix E) regarding the relationship between the Domino Effect Parameter DEP and the mean airspace density. It is hypothesised that, in local airspace operating above its capacity limits and using speed-based conflict resolution with decelerations only, all local aircraft continuously fly close to the minimum airspeed due to the large number of conflicts. Hence, limited additional resolution manoeuvres are performed by these aircraft, preventing the increase of the DEP with density. Additional research is required to validate this hypothesis.

A partial solution for preventing instability would be to disallow traffic to stand still on an intersection, similar to rules in road transportation. In that case, crossing the intersection is still possible for the traffic of the non-blocked airway, as long as no aircraft desires to turn into the blocked airway. To also solve the turning traffic problem, turning lanes or altitude layers would need to be included, such as in Doole et al. [5].

D.3. Flow rate proportions in the two-dimensional orthogonal grid network

The discussion of Section 7 stated that the flow ratio at the four busy intersections near the centre of the two-dimensional orthogonal grid network airspace is unbalanced in the experiments, i.e., approximately $1.7:1$. This appendix includes a diagram of the proportional flow rates in each network leg of the grid network airspace to substantiate these numbers.

The flow rates are extracted by randomly generating $10,000$ routes through the grid network, following the assignment of the origin and destination nodes and the routing algorithm as discussed in Section 5. Hence, the flow proportions presented in this appendix are not exact calculations but em-

pirical approximations of the mean. The empirical flow rates of the $10,000$ routes are normalised, such that the sum of all proportional flow rates equals 1. Therefore, to model an experiment run, the mean flow rates in each network leg can be obtained by multiplying the proportional flow rates and the desired mean departure rate $\overline{q}$ of Equation (25). In Figure 20, the flow proportions are shown. Due to rounding of the flow proportions, the sum of all flow proportions does not necessarily equal 1 in this figure.

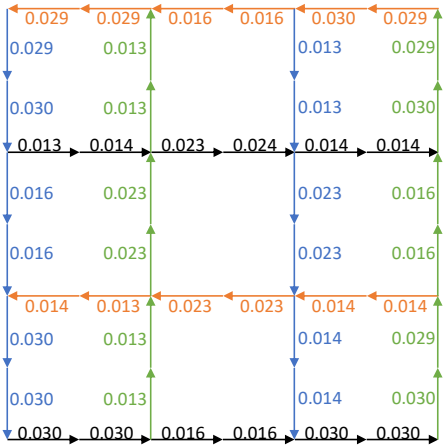

Figure 20: Flow proportions per leg of the two-dimensional orthogonal grid network airspace

E. Analytical conflict count models for constrained urban airspace

In the Metropolis project (Sunil et al. [23, 24]), three conflict-based metrics are defined: safety, efficiency, and stability. In this paper, the efficiency metric was assessed using the Macroscopic Fundamental Diagram. To improve understanding of the factors influencing the safety and stability metrics, this appendix presents an adaptation of the analytical conflict count models developed by Sunil et al. [25, 26] for general airspace. The derived conflict count models for constrained urban airspace are validated using the fast-time simulation experiment scenarios of Section 5 and Appendix B.1.

This appendix is structured in four parts. Firstly, a short overview of the three metrics is given. Next, the model derivations are presented. Subsequently, similar to the model for the Macroscopic Fundamental Diagram, these models are validated using a comparison with fast-time simulation experiments on a single intersection and in a grid network environment. Lastly, a short discussion on the results is included.

E.1. Measuring airspace safety and stability

Airspace safety is assessed by two metrics: *intrinsic* and *true* safety. Intrinsic safety focuses on the safety provided by the constraints and design of the airspace, e.g., buildings and one-way airways. Intrinsic safety is ranked by the number of conflicts without conflict resolution manoeuvres. However, while a highly structured environment can better prevent conflicts from occurring, it simultaneously limits the resolution possibilities for the remaining conflicts. Therefore, next to the intrinsic safety metric, the true safety metric is used. True safety is evaluated by the number of conflicts when conflict resolution manoeuvres are performed, thereby representing safety in an actual environment.

Airspace stability is represented by the Domino Effect Parameter DEP (Bilimoria et al. [1], Jardin [15], Sunil et al. [25]). Conflict resolution manoeuvres may lead to new conflicts with other aircraft. For example, such chain reactions are resembled by the formation of queues in the constrained urban airspace. As noted in Section 3, these chain reactions can propagate through an entire network and lead to the constrained urban airspace becoming unstable. The DEP measures the proportion of conflicts occurring due to such chain reactions. Therefore, it is a metric for airspace stability. It is defined as a function of the total number of conflicts with conflict resolution $C_{total,WR}$ and the number with no conflict resolution $C_{total,NR}$ (Sunil et al. [25]):

$$DEP = \frac{C_{total,WR}}{C_{total,NR}} - 1 \tag{31}$$

E.2. Analytical conflict count model derivations

This section starts with the derivation of an analytical conflict count model for an environment without conflict resolution. This model is used in combination with the delay model presented in Section 4 to derive a with resolution conflict count model. Again, consider the intersection of Figure 4. The arrival of vehicles in each upstream leg is assumed to be given by a Poisson process. However, in an environment with conflict resolution, two aircraft from the same upstream leg do not arrive simultaneously at an intersection, as their distance separation is at least equal to the horizontal separation requirement S_h. Therefore, for both a no resolution (NR) and a with resolution (WR) environment, the distance separation between each vehicle within an airway is expected to be represented by an exponential distribution, shifted to include a minimum distance of S_h. The cumulative density function of the distance separation $D_{\parallel}$ in an upstream leg u is given by:

$$P(D_{\parallel} \leq x) = \begin{cases} 0 & x \leq S_h \\ 1 - (1 - S_h q_u) e^{-q_u (x - S_h)} & x > S_h \end{cases} \tag{32}$$

E.2.1. Analytical conflict count model for an environment without conflict resolution

For many non-constrained airspaces, analytical conflict count models have been proposed using the *gas model*, as derived and extended by Datta and Oliver [3], Endoh [6], Graham and Orr [10] and Sunil et al. [26]. The name refers to the combinatorial characteristic inherent to any system where all moving particles are equally likely to meet each other (Sunil et al. [26]). In airspace capacity research, the moving particles are the aircraft, while the system is the airspace. The gas model will be used as the starting point for the derivation of an analytical conflict count model for constrained urban airspace. It states that the number of instantaneous conflicts NR $C_{i,NR}$ for a pairwise interaction is a function of the number of pairwise combinations and the probability of conflict per pair for that interaction (Sunil et al. [26]):

$$C_{i,NR}(interaction) = No.of\ combinations \cdot \frac{2 S_h \overline{V_r} t_l}{A} \tag{33}$$

In this equation, S_h represents the horizontal separation requirement, $\overline{V_r}$ the mean relative velocity, and t_l the look-ahead time. When all aircraft fly at equal cruise velocity V_{NR}, $\overline{V_r}$ is a function of the absolute difference between the ground track angles ψ of both flows (Sunil et al. [26]):

$$\overline{V_r} = 2 V_{NR} \sin(|\Delta\psi|/2) \tag{34}$$

Equation (33) needs to be applied to all pairwise interactions happening in the airspace. For the single orthogonal intersection of Figure 4, the number of instantaneous conflicts can be split into the interaction between aircraft from both flows C_+, and the interactions between traffic within each leg $C_{\parallel,f}$:

$$C_{i,NR} = C_{i+,NR} + \sum_{f \in F} C_{i\parallel,NR,f} \tag{35}$$

By Equation (34), the relative velocity between two aircraft travelling within the same airway is zero, i.e., $\overline{V_{r\parallel}} = 0$, leading to $C_{i\parallel,NR,f}$ being zero for all four legs. In other words, two such aircraft are either in an instantaneous intrusion or not, but will not detect any conflict between them. Therefore, Equation (35) is dependent on the number of instantaneous crossing conflicts $C_{i+,NR}$ only.

Consider the two airspaces in Figure 21, with two flows parallel to either side. Endoh [6] proved that for any rhombus-shaped airspace with two crossing flows, $C_{i+,NR}$ is independent of the aircraft being constrained within an airway (Figure 21b) or not (Figure 21a). Namely, for the constrained airspace of Figure 21b, the area eligible for a crossing intrusion is reduced significantly. At the same time, however, the number of instantaneous combinations possible within that area is reduced by the same factor, cancelling out each other in Equation (33). Therefore, as all parameters in the numerator of the conflict probability of Equation (33), S_h, $\overline{V_r}$, and t_l, are equal for both airspaces, $C_{i+,NR}$ is identical for any parallelogram-shaped airspace, regardless of the flows being constrained or free.

Only the aircraft within both upstream legs of the intersection can detect crossing conflicts at the intersection. Therefore, the mean numbers of instantaneous aircraft in the two upstream legs $\overline{N_{i,u}}$ are used to determine the number of combinations. If equal length is assumed for all four legs, the upstream

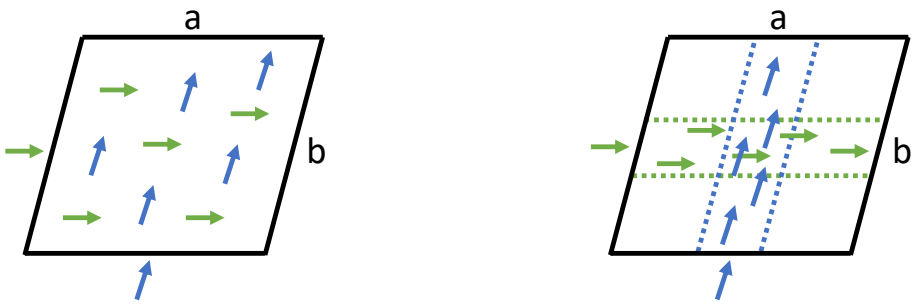

(a) Free airspace (b) Constrained airspace

Figure 21: A free and a constrained parallelogram-shaped airspace of equal area $A(= a \cdot b)$ with two crossing flows parallel to the sides, where $C_{i+,NR}$ is equal in both airspaces

$\overline{N}_{i,u}$ can be copied downstream (i.e., doubled), as if no turning traffic is present. Hence, the number of combinations is given by:

$$No.of\ combinations = \prod_{u \in U} 2\overline{N}_{i,u} \tag{36}$$

And, in case no turning traffic is present, the number of instantaneous crossing conflicts $C_{i+,NR}$ can be obtained by substituting Equation (36) into Equation (33):

$$C_{i+,NR} = \frac{8S_h\overline{V}_{r+}t_l}{A}\prod_{u \in U}\overline{N}_{i,u} \tag{37}$$

Recall the discussion on turning traffic from Section 3. Case 2 turning traffic, with aircraft turning into the airway, decreases the conflict duration, as the aircraft turns out of conflict before the intrusion. Therefore, the instantaneous number of crossing conflicts is overestimated when accounting for case 2 turning traffic. However, considering that the mean conflict duration t_c would be equal to the look-ahead time t_l if the aircraft had not turned, the total number of crossing conflicts NR can still be predicted by the model. $C_{total+,NR}$ is given by multiplying $C_{i+,NR}$ with the analysis time interval T and dividing by the mean conflict duration t_c, which is equal to t_l (Sunil et al. [25]):

$$\begin{aligned} C_{total+,NR} &= \frac{C_{i+,NR}T}{t_c} \\ &= \frac{8S_h\overline{V}_{r+}T}{A}\prod_{u \in U}\overline{N}_{i,u} \end{aligned} \tag{38}$$

The other situation, i.e., case 1 turning traffic, with aircraft turning out of the airway, has an increasing impact on the total number of conflicts. Each aircraft following within a distance $S_{h,\angle}(\Delta\psi)$ of an aircraft turning out of its airway adds one conflict to the total. As a result, the total number of conflicts NR extra generated by turning traffic is a function of the probability that an aircraft is within a distance $S_{h,\angle}(\Delta\psi)$, given by Equations (2) and (32), as the Poisson flow is memoryless. This probability needs to be multiplied by the total number of turning aircraft, which is the product of the turn probability within an upstream leg $P(turn_u)$, and the total number of aircraft within an upstream leg $N_{total,u}$:

$$C_{total,turn,NR} = \sum_{u \in U} P(D_{\parallel,u} \leq S_{h,\angle}(\Delta\psi)) \cdot P(turn_u) \cdot N_{total,u} \tag{39}$$

And the total number of conflicts NR $C_{total,NR}$ for a single intersection equals:

$$C_{total,NR} = C_{total+,NR} + C_{total,turn,NR} \tag{40}$$

E.2.2. Analytical conflict count model for an environment with conflict resolution

An aircraft that incurs a delay remains in the local airspace in front of the intersection longer. The total delay incurred per second $\dot{d}$ equals the mean number of vehicles queueing in an upstream leg u and

is, therefore, given by Little's law (Little [18]):

$$\dot{d}_u = \overline{d}_u \overline{q}_u \tag{41}$$

Each aircraft arriving at the intersection during the delay of the decelerated aircraft encounters a conflict with that aircraft or, when queues get longer, with an aircraft further down the queue. Nevertheless, a conflict will be detected. Therefore, to obtain the rate of queueing conflicts $\dot{C}_q$, $\dot{d}$ needs to be multiplied by the mean number of aircraft arriving per second at the intersection $\overline{q}_+$:

$$\dot{C}_{q,u} = \dot{d}_u \overline{q}_+ = \overline{d}_u \overline{q}_u \overline{q}_+ \tag{42}$$

Subsequently, the total number of queueing conflicts on an intersection $C_{total,q}$, generated by conflict resolution, can be determined by summing $\dot{C}_{q,u}$ for the set of upstream legs U and multiplying by the analysis time interval T:

$$C_{total,q} = T \sum_{u \in U} \overline{d}_u \overline{q}_u \overline{q}_+ \tag{43}$$

The mean flow rates are unchanged by conflict resolution (see Section 3). Therefore, an equal number of crossing and turning conflicts compared to the environment without conflict resolution is detected. Hence, the total number of conflicts with resolution $C_{total,WR}$ is given by the sum of the NR conflict count and the queueing conflicts:

$$C_{total,WR} = C_{total,NR} + C_{total,q} \tag{44}$$

Note that all derivations presented in this section are valid for intersections both without as well as with turning traffic, taking Assumption 2 into account. Furthermore, as all conflicts are pairwise, conflicts only occur at one intersection at the same time. Therefore, most of the behaviour in an urban grid network can be approximated by the sum of all separate intersections. However, two differences with single intersections need to be considered: departures and arrivals within the airspace and the flow rate distribution of arriving flows at an intersection.

Firstly, departures and arrivals take place within the airspace. As a result, the constrained conflict equivalence of Figure 21 cannot be applied to the entire airspace. However, it is still valid for single intersections. In this paper, traffic departs and arrives at a node halfway between two intersections with the same velocity and altitude as the cruising traffic. For the departing traffic, this means that these nodes act as an intersection of an upstream and a downstream leg containing cruising traffic and one departing leg towards that node. This departing traffic leg has zero length, i.e., $N_{i,NR} = 0$ (see Equation (5)). In addition, as the departing traffic instantly flies at cruise speed, it can only experience an instant intrusion with cruising aircraft and no conflicts, i.e., for departures $C_{total,NR} = 0$. With resolution, such a node can be modelled equivalent to a regular intersection, using Equation (21) for the mean delay $\overline{d}$ and Equation (44) for the total number of conflicts WR $C_{total,WR}$. See Appendix C for a further analysis on departure traffic in the grid network environment.

Secondly, in the derivation of $C_{total,turn,NR}$ of Equation (39) for a single intersection, it is assumed that the arriving flows were deconflicted before departure. In a network without conflict resolution, this is not the case. Instead, the flows are assumed to be represented by a pure (non-shifted) Poisson process. Hence, the cumulative probability distribution of the flow in any upstream leg of an intersection in a grid network (subscript ⊞) given by the exponential distribution of the mean upstream flow rate $\overline{q}_u$:

$$P(D_{\parallel,\boxplus,u} \leq x) = \begin{cases} 0 & x \leq 0 \\ 1 - e^{-\overline{q}_u x} & x > 0 \end{cases} \tag{45}$$

On the one hand, without conflict resolution, each aircraft within a distance of S_h is in an intrusion and, therefore, will not experience a conflict. Accordingly, $C_{total,turn,NR,\boxplus}$ is given by subtracting these aircraft from the separation distance probability to obtain the total number for a single intersection, and summing that for each intersection i in the set of intersections I:

$$C_{total,turn,NR,\boxplus} = \sum_{i \in I} \sum_{u \in U(i)} \left(P(D_{\parallel,\boxplus,u} \leq S_{h,\angle}(\Delta\psi)) - P(D_{\parallel,\boxplus,u} \leq S_h) \right) \cdot P(turn_u) \cdot N_{total,u} \tag{46}$$

On the other hand, with conflict resolution, the traffic will arrive separated, similar to the single intersection case. Hence, $C_{total,turn,WR,\boxplus}$ is equal to $C_{total,turn,NR}$ for the single intersection (defined by Equation (39)), summed for all intersections:

$$C_{total,turn,WR,\boxplus} = \sum_{i \in I} C_{total,turn,NR}(i) \tag{47}$$

The number of crossing conflicts NR $C_{total+,NR}$ is not impacted by both changes. All in all, using $n \in N$ for node n in the set of all network nodes N (i.e., the union of the set of all intersection nodes I and the set of all OD-nodes), the two analytical grid network conflict count models are given by:

$$C_{total,NR,\boxplus} = C_{total,turn,NR,\boxplus} + \sum_{i \in I} C_{total+,NR}(i) \tag{48}$$

$$C_{total,WR} = \sum_{i \in I} \left(C_{total+,NR}(i) + C_{total,turn,NR}(i) \right) + \sum_{n \in N} C_{total,q}(n) \tag{49}$$

E.3. Comparison of analytical conflict count models with fast-time simulation experiments

This section compares the analytical estimations for the conflict counts with the results of the fast-time simulation experiments for the four single intersection experiments of Appendix B.1 and for the three orthogonal grid network simulation experiments of Section 5. A figure is shown per variable and set of experiments to inspect the similarity in shape and magnitude. In all figures, the experimental results of the simulations are marked as scatter points with an 'x', while the prediction of the analytical model is shown as a solid line of the same colour. Additionally, a table is included to show the values for k and $k_{\%}$ of Equations (26) and (27) for each comparison.

First, this section compares the predictions of the two analytical conflict count models, derived in this appendix, and the results of the fast-time simulation experiments for the single intersection environment. At the same time, model accuracy is validated for the turning traffic experiment. Next, the similarity between the analytical conflict count models and the simulation experiments for the orthogonal grid network is shown.

E.3.1. Accuracy of conflict count models in the single intersection environment

Figure 22 and Table 11 show the comparison between the analytical model predictions and the simulation experiment results for the total number of conflicts without conflict resolution on the intersection. The comparison shows that for all three flow ratios, the analytical model of Equation (40) can closely predict both the shape and magnitude of the experimental data over the entire range of densities.

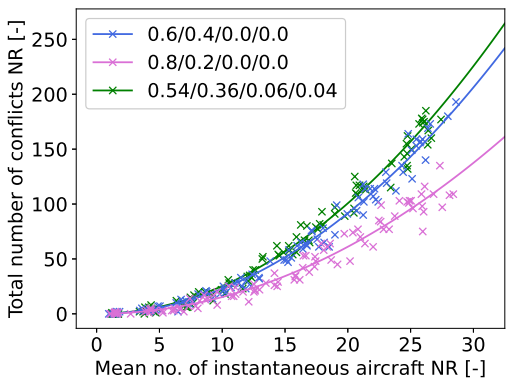

Figure 22: Comparison between the analytical conflict count model (solid line) and the fast-time simulation experiments (x) for $C_{total,NR}$ on the intersection

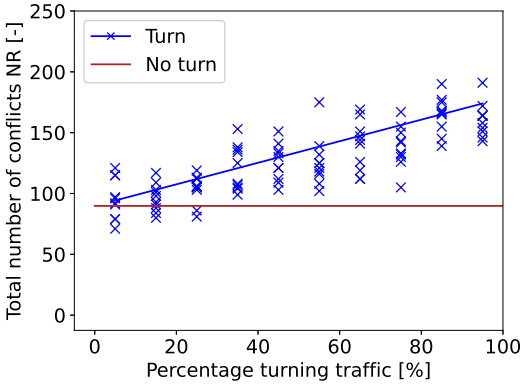

Figure 23: Comparison between the analytical conflict count model (solid line) and the fast-time simulation experiment (x) for $C_{total,NR}$ per turn percentage with as base flow ratio $(0.6/0.4/0/0)$ and $q_+ = 0.7 s_+$

The comparison of $C_{total,NR}$ for the turning traffic experiment is shown in Figure 23. The analytical model again closely predicts the shape and magnitude of the experimental results. The value for $k_{\%}$

Table 11: Accuracy of the analytical conflict count model for $C_{total,NR}$ on the intersection

Flow ratio	k	$k_{\%}$
$(0.6/0.4/0/0)$	1.00	100%
$(0.8/0.2/0/0)$	1.01	99.5%
$(0.54/0.36/0.06/0.04)$	0.984	98.3%
Turn experiment	0.947	94.4%

of almost 95% demonstrates this as well. In addition, the experiment confirms that extra conflicts are generated when more turning traffic is present.

Figure 24 and Table 12 show the comparison of the model of Equation (44) with the total number of conflicts WR extracted from the experiments. For the more balanced flows ($(0.6/0.4/0/0)$ and $(0.54/0.36/0.06/0.04)$), the analytical model shows a strong correlation with the experimental data over the entire range of densities, with a $k_{\%}$ higher than 98%. However, when the flow is less balanced (validated by the $(0.8/0.2/0/0)$ experiment), the model significantly overestimates the number of conflicts WR for the highest densities. This overestimation can partly be explained by the analytical delay model overestimating the experimental results for high densities for this flow ratio, as shown in Figure 8.

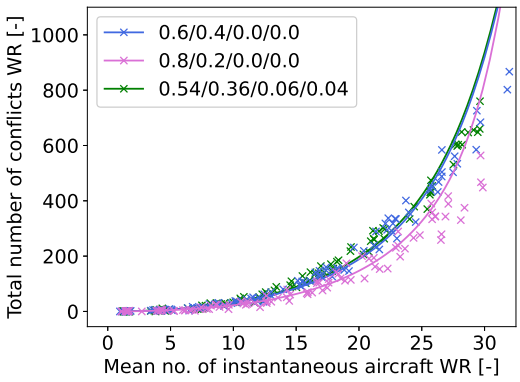

Figure 24: Comparison between the analytical conflict count model (solid line) and the fast-time simulation experiment (x) for $C_{total,WR}$ on the intersection

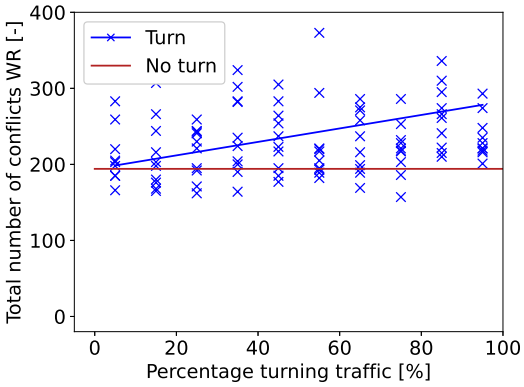

Figure 25: Comparison between the analytical conflict count model (solid line) and the fast-time simulation experiment (x) for $C_{total,WR}$ per turn percentage with as base flow ratio $(0.6/0.4/0/0)$ and $q_+ = 0.7 s_+$

Table 12: Accuracy of the analytical conflict count model for $C_{total,WR}$ on the intersection

Flow ratio	k	$k_{\%}$
$(0.6/0.4/0/0)$	0.984	98.4%
$(0.8/0.2/0/0)$	0.727	62.5%
$(0.54/0.36/0.06/0.04)$	1.01	98.6%
Turn experiment	0.950	94.8%

Looking at $C_{total,WR}$ for the turn experiment in Figure 25, the increasing effect seen in Figure 23 for the experimental data is not equally present in the experimental results. Therefore, the model is less accurate, as shown in Table 12. Nevertheless, a value of more than 90% indicates that the magnitude of the total number of conflicts is still well predicted.

Lastly, the results for the domino effect parameter for the intersection experiments are shown. Here, Figure 26 visually compares the accuracy, while the k accuracies are summarised in Table 13. The analytical model can predict the DEP at balanced intersections with an accuracy level of 90% and above, while for the unbalanced intersection of $(0.8/0.2/0/0)$ the model significantly overestimates the experimental data.

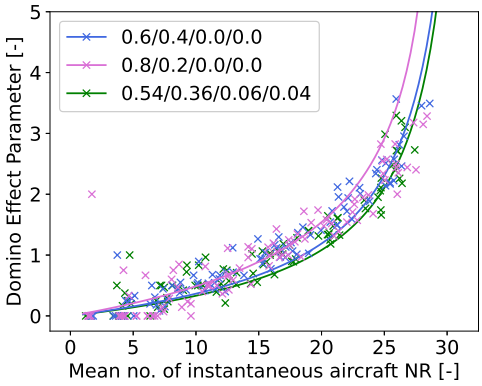

Figure 26: Comparison between the analytical model (solid line) and the fast-time simulation experiment (x) for the DEP of the intersection experiments

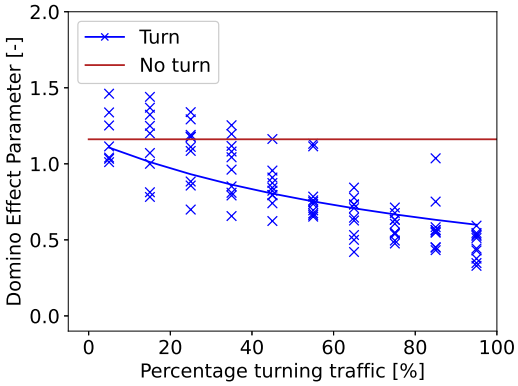

Figure 27: Comparison between the analytical conflict count model (solid line) and the fast-time simulation experiment (x) for DEP per turn percentage with as base flow ratio $(0.6/0.4/0/0)$ and $q_+ = 0.7s_+$

Table 13: Accuracy of the analytical model for the DEP compared to the single intersection experiments

Flow ratio	k	$k_{\%}$
$(0.6/0.4/0/0)$	1.03	97.4%
$(0.8/0.2/0/0)$	0.714	59.9%
$(0.54/0.36/0.06/0.04)$	1.09	91.6%
Turn experiment	1.07	93.5%

E.3.2. Accuracy of conflict count models in the orthogonal grid network environment

Table 14 and Figures 28 to 30 show the comparison between the three conflict count variables for the orthogonal grid experiments and the analytical model of Equations (31), (48) and (49).

For the total number of conflicts NR, the analytical model underestimates the magnitude of the base and $2S_h$ experiments by a factor of 16.5% and 19.7%, respectively. Meanwhile, for the $0.5V_{NR}$ experiment, an overestimation is seen of 12.7%. Still, the shape of the experiments is closely approximated by the analytical model.

Likewise, for the total number of conflicts WR, the shape of the experimental data closely aligns the analytical model's prediction. However, the magnitude of $C_{total,WR}$ is overestimated by the model for all three experiments. The largest overestimation is found for the $0.5V_{NR}$ experiment, which can be explained by the overestimation seen for $C_{total,NR}$ for this experiment. By Equation (44), $C_{total,NR}$ is a major factor in the analytical model for $C_{total,WR}$.

The shown inaccuracies of the analytical model for both conflict count variables result in a significant overestimation of the experimental results for the Domino Effect Parameter (consider Equation (31)). The magnitude of the overestimation is indicated by a $k_{\%}$ of 40.1% and lower. Interestingly, both the analytical model predictions and the simulation results for the base experiment overlap with the analytical model for the $0.5V_{NR}$ experiment.

Table 14: Accuracy of the analytical conflict count models for the three grid network experiments

	Base		$0.5V_{NR}$		$2S_h$	
Variable	k	$k_{\%}$	k	$k_{\%}$	k	$k_{\%}$
$C_{total,NR}$	1.20	83.5%	0.888	87.3%	1.25	80.3%
$C_{total,WR}$	0.862	84.0%	0.653	46.7%	0.845	81.7%
DEP	0.530	11.4%	0.625	40.1%	0.491	−3.66%

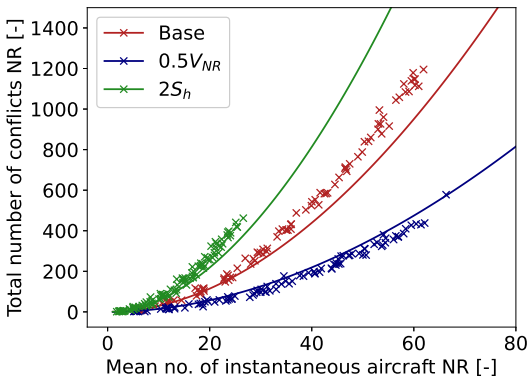

Figure 28: Comparison between the analytical conflict count model (solid line) and the fast-time simulation experiment (x) for $C_{total,NR}$ for the orthogonal grid network experiments

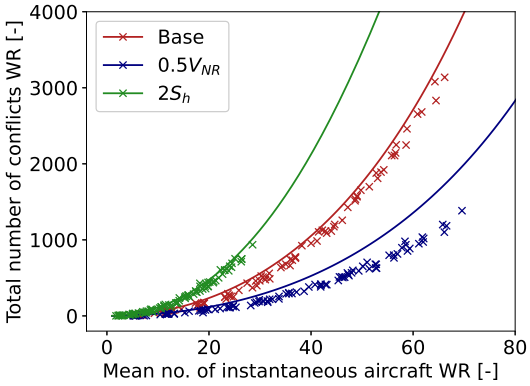

Figure 29: Comparison between the analytical conflict count model (solid line) and the fast-time simulation experiment (x) for $C_{total,WR}$ for the orthogonal grid network experiments

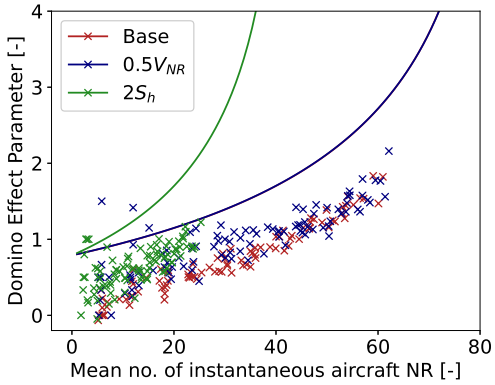

Figure 30: Comparison between the analytical conflict count model (solid line) and the fast-time simulation experiment (x) for the DEP for the orthogonal grid network experiments. The analytical model for the Base experiment is not seen, as it overlaps with the model for the $0.5V_{NR}$ experiment

E.4. Discussion on the findings of conflict count models

The comparison of the fast-time simulation experiment results and the analytical models for the single intersection environment showed that model accuracy was generally high for both safety parameters, with accuracies of more than 90%. Only when predicting the conflict count with resolution at a less balanced intersection (experiment $(0.8/0.2/0/0)$), the analytical model showed a significant overestimation. This overestimation results from the overestimation in the analytical delay model for the same experiment, as was seen in Appendix B. In turn, this error in the analytical delay model is caused by an overestimation of the red time, as discussed in Section 7.

The analytical conflict count model correctly predicted the shape of $C_{total,NR}$ and $C_{total,WR}$ for the grid network. The resulting domino effect parameter is predicted less accurately, overestimating the experimental data for all three experiments. A significant difference exists between the level of accuracy in estimating the total number of conflicts NR for $C_{total,NR}$ of the Base and $2S_h$ experiments versus the $0.5V_{NR}$ experiment. It is expected that this difference in accuracy is caused by arriving traffic predicting conflicts at the intersection downstream of their destination. In the grid network experiment, the distance between an OD-node and the intersection is 200m, coincidentally equal to the look-ahead time multiplied by the cruise speed V_{NR}. As a result, moments before arrival, conflicts at the downstream intersection are already detected. The overestimation confirms this for $C_{total,NR}$ of the $0.5V_{NR}$ experiment. In the $0.5V_{NR}$ experiment, the look-ahead time does not reach downstream intersections. As the level of accuracy in estimating $C_{total,NR}$ is lowered, the level of accuracy in the approximation of $C_{total,WR}$ and the DEP is decreased as well.

For the total number of conflicts with resolution, the analytical model overestimates the results of all three grid network experiments. This overestimation was seen in the single environment for unbalanced

intersections. As shown in Appendix D.3, the four busy intersections in the centre of the grid network environment are unbalanced, resulting in an overestimation for the entire network.

As false conflicts were present in the Base and $2S_h$ experiments, the domino effect parameter's accuracy is strongly impacted. Nevertheless, even for the $0.5V_{NR}$ experiment, the strong overestimation of the analytical model for the total number of conflicts WR results in a level of accuracy for the DEP of 40% only. As the DEP is the combination of both conflict count models, the analysis presented above holds for the DEP as well. Altogether, despite the discussed model inaccuracies, the analytical model showed to be well capable of estimating the conflict count on single intersections and, more limited, on an orthogonal grid network.

F. Miscellaneous other model derivations

During the derivation of the analytical models for mean delay and conflict counts, as presented in Section 4 and Appendix E.2, several extra models were derived. Future research may benefit from the derivations presented in this appendix. Firstly, a general no resolution conflict count model is described, where the number of conflicts within an airway is determined when the equal cruise speed assumption is dropped. Secondly, a no resolution intrusion count model is derived and validated.

F.1. General no resolution conflict count model

In Appendix E.2.1, the NR conflict count model was derived assuming equal cruise velocities for all aircraft. Hence, the relative velocities within an airway are zero, leading to the number of conflicts within a flow $C_{i\parallel,NR}$ being non-existent. However, also when the relative velocity within an airway is non-zero, the number of conflicts within a flow can be modelled using Equation (33).

For large $\overline{N}_{i\parallel}$, the number of combinations can be approximated by $\binom{N_{i\parallel}}{2}$ multiplied with the conflict probability (Sunil et al. [26]). Yet, for smaller areas or low densities, the possibility exists that, on average less than one aircraft is present, yielding a negative number of combinations. Therefore, a new approximation is proposed, based on the assumption that the flow behaves similar to a stochastic Poisson process with mean $\overline{N}_{i\parallel}$. By summation of all Poisson probabilities that x equals n, respectively multiplied by the gas model for $\overline{N}_i = n$, the gas model for within airway conflicts $C_{i\parallel,f,NR}$ becomes:

$$C_{i\parallel,NR,f} = \sum_{n=2}^{\infty} P(X=n)\frac{n(n-1)}{2}\frac{2S_h\overline{V}_{r\parallel}t_l}{A_{\parallel}}, \qquad X = Poisson(\overline{N}_{i\parallel}) \tag{50}$$

Note: this equation needs to be performed on the flow f in each arm of an intersection separately, and summed afterwards:

$$C_{i\parallel,NR} = \sum_{f\in F} C_{i\parallel,NR,f} \tag{51}$$

In the conflict count model, Equation (51) needs to be inserted into Equation (35), and all other equations used as shown in Appendix E.2.1. The resulting model is validated through the intrusion model shown in Figure 31, where the intrusion count equivalent of Equation (51) is used to determine the instantaneous number of intrusions. In this figure, the model closely follows both the shape and magnitude of the experimental data, confirming the accuracy of Equation (51).

F.2. No resolution intrusion count model

For modelling of the instantaneous number of intrusions NR $I_{i,NR}$ in the single intersection environment of Figure 4, a minor adjustment needs to be made to the gas model of Equation (33). Instead of the swept area $2S_h\overline{V}_r t_l$, the area of the protected zone $\pi {S_h}^2$ needs to be used:

$$I_{i,NR} = No.of\ combinations \cdot \frac{\pi {S_h}^2}{A} \tag{52}$$

Similar to the NR conflict count model, intrusions are pairwise, meaning that the model needs to be split into the different interactions of crossing intrusions I_+ and within airway intrusions $I_\parallel$ for all legs f of the intersection:

$$I_{i,NR} = I_{i+,NR} + \sum_{f \in F} I_{i\|,NR,f} \tag{53}$$

Then, using the substitution shown in Equation (52) for Equations (37) and (50), the complete instantaneous intrusion model can be derived.

Next, to model the total number of intrusions, consider that in an NR airspace, by definition, each conflict eventually results in an intrusion. One exception exists when the state-based conflict detection algorithm detects a false conflict, often due to a change in direction by one aircraft (arrivals could cause false conflicts as well). The set of aircraft experiencing this change in direction was called case 2 turning traffic in Section 3.2. Following their planned route, aircraft can avoid an intrusion by performing a turn. Therefore, the total number of intrusions NR is given by:

$$I_{total,NR} = C_{total,NR} - I_{total,turn,avoided,NR} \tag{54}$$

As the number of intrusions is not relevant for the capacity metrics used in this study, no model for $I_{total,turn,avoided,NR}$ is derived, and this value is set at 0 in the comparison below. Hence, it is expected that the analytical model overestimates the total number of intrusions when turning traffic is present. The comparison between the model and the three intersection experiments is shown in Figures 31 and 32 and Table 15. As can be seen, the model is accurate for both cases without turns. With turns, the number of instantaneous intrusions is significantly higher, as aircraft turning into an airway and an intrusion simultaneously remain in that intrusion for their entire remaining flight time. Hence, the average intrusion duration is increased significantly, increasing $I_{i,NR}$. This is not included in the model. Analogous to the derivation of the NR conflict count model in Appendix E.2.1, turns do not impact $I_{total,NR}$ for low to medium densities. The lower accuracy, i.e., $k = 0.951$, for the $(0.54/0.36/0.06/0.04)$ experiment indicates that $I_{total,turn,avoided,NR}$ should be accounted for.

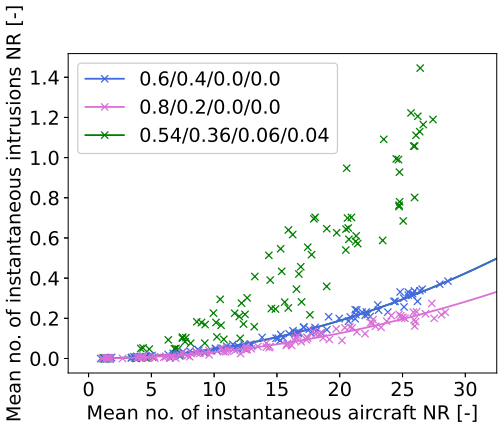

Figure 31: Comparison between the analytical model (solid line) and the fast-time simulation experiment (x) for $I_{i,NR}$ on the intersection (the analytical model for the $(0.54/0.36/0.06/0.04)$ experiment overlaps with the model for the $(0.6/0.4/0/0)$ experiment, and is thereby not visible)

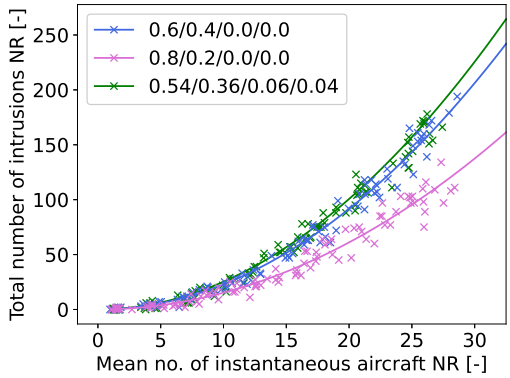

Figure 32: Comparison between the analytical model (solid line) and the fast-time simulation experiment (x) for $I_{total,NR}$ on the intersection

Table 15: Accuracy of the model for $I_{i,NR}$ and $I_{total,NR}$ on the intersection

	$I_{i,NR}$		$I_{total,NR}$	
Flow ratio	k	$k_{\%}$	k	$k_{\%}$
$(0.6/0.4/0/0)$	0.998	99.8%	1.00	99.9%
$(0.8/0.2/0/0)$	1.00	99.6%	1.00	99.6%
$(0.54/0.36/0.06/0.04)$	3.291	30.4%	0.951	94.8%

G. Miscellaneous results

In this appendix, miscellaneous comparisons between the analytical model predictions and the results of the fast-time simulation experiments are shown. Firstly, the analytical instantaneous conflict count model is validated. Next, a short investigation into the accuracy of the delay model in predicting the delay in a single upstream leg is presented. Finally, this appendix concludes by evaluating the accuracy of the analytical models in approximating behaviour in the orthogonal grid network for five variables: the number of instantaneous intrusions NR $I_{i,NR}$, the total number of intrusions NR $I_{total,NR}$, the mean delay $\overline{d}$, the mean velocity WR V_{WR}, and the mean speed WR $N_{i,WR}$.

G.1. Comparison of the analytical instantaneous conflict count model

For the model in the instantaneous number of conflicts NR, Equation (37) is used. For this equation, turning traffic is assumed to have an equal impact on $C_{i,NR}$ as non-turning traffic. This assumption is an approximation, as turning aircraft conflicts are present. However, these conflicts have a relatively short duration, resulting in only a slight deviation in $C_{i,NR}$. The sum of the instantaneous number of conflicts NR for all intersections and departure nodes predicted by Equation (37) is used to analytically predict the instantaneous number of conflicts in the orthogonal grid network airspace.

The comparison is shown in Figures 33 and 34 and Table 16. The accuracy level is very high for all single intersection experiments and all grid network experiments, with $k_{\%}$ accuracies of 95% and above. However, only if the average conflict duration t_c is known, the total number of conflicts can be determined using (Sunil et al. [25]):

$$C_{total,NR} = \frac{C_{i+,NR}T}{t_c} \tag{55}$$

As discussed in Appendix E, the average conflict duration is lower than the look-ahead time as turning traffic is present. In addition, departures and arrivals in the grid network environment lower the average conflict duration. Therefore, the observed high accuracy for the number of instantaneous conflicts cannot be converted directly into a high accuracy total conflict count model.

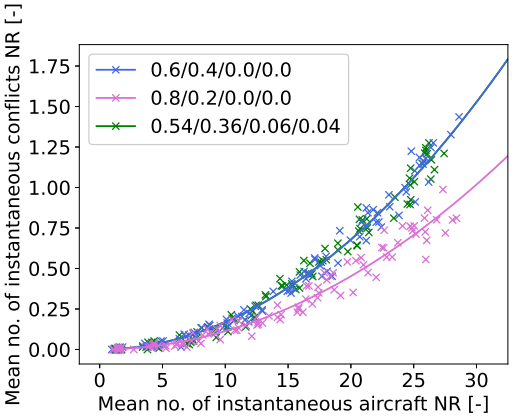

Figure 33: Comparison between the analytical model (solid line) and the fast-time simulation experiment (x) for $C_{i,NR}$ for the intersection experiments (the analytical model for the $(0.54/0.36/0.06/0.04)$ experiment overlaps with the model for the $(0.6/0.4/0/0)$ experiment, and is thereby not visible)

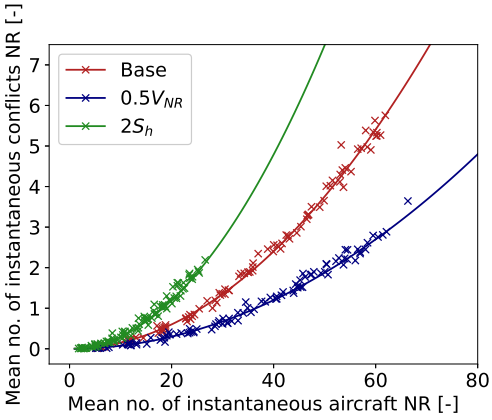

Figure 34: Comparison between the analytical model (solid line) and the fast-time simulation experiment (x) for $C_{i,NR}$ for the grid network experiments

G.2. Accuracy of the analytical model in predicting the delay in a single upstream leg

To validate the mean delay in an upstream leg $\overline{d}_u$ of Equation (9) specifically, Figures 35 and 36 show the mean delay split per upstream leg of the $(0.6/0.4/0/0)$ and $(0.8/0.2/0/0)$ experiments, respectively. The accuracies are summarised in Table 17. As hypothesised in the discussion (Section 7), the northbound 0.2 leg shows significant overestimation for higher values of $\overline{d}$, as the red time of the eastbound 0.8 flow is overestimated. The observed underestimations for higher densities can be explained by the random nature of arrivals, as discussed in Appendix B.2. In short, the analytical delay

Table 16: Accuracy of the model for $C_{i,NR}$ on the intersection and on the grid network

Experiment	k	$k_{\%}$
$(0.6/0.4/0/0)$	1.00	99.9%
$(0.8/0.2/0/0)$	1.00	99.7%
$(0.54/0.36/0.06/0.04)$	0.997	99.7%
Base	1.00	99.8%
$0.5V_{NR}$	1.03	97.2%
$2S_h$	1.04	95.9%

model does not scale linearly with the mean density. Therefore, an analytical prediction using the mean density will underestimate the mean delay.

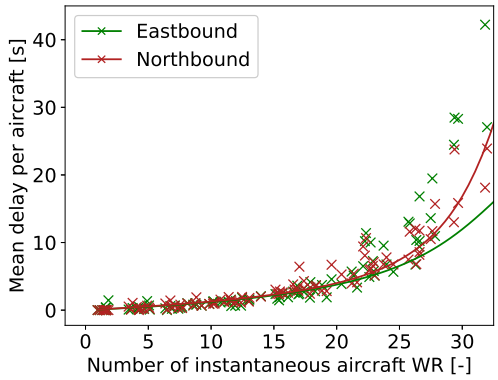

Figure 35: Comparison between the analytical model (solid line) and the fast-time simulation experiment (x) for $\overline{d}$ per flow of the $(0.6/0.4/0/0)$ experiment

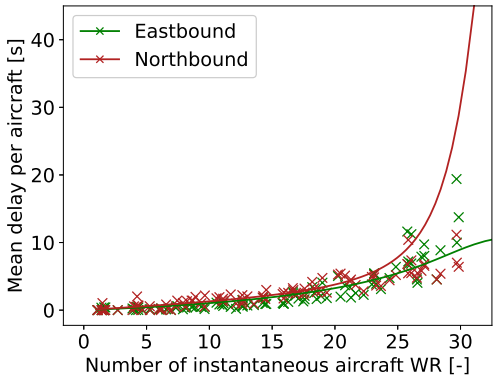

Figure 36: Comparison between the analytical model (solid line) and the fast-time simulation experiment (x) for $\overline{d}$ per flow of the $(0.8/0.2/0/0)$ experiment

Table 17: Accuracy of the model for $\overline{d}$ per flow on the intersection

Flow ratio	Flow: ratio	k	$k_{\%}$
$(0.6/0.4/0/0)$	East: 0.6	1.88	53.3%
	North: 0.4	1.22	81.9%
$(0.8/0.2/0/0)$	East: 0.8	1.12	89.4%
	North: 0.2	0.407	−45.8%

G.3. Orthogonal grid network experiment

For the grid experiment, several plots shown for the intersection experiment were not presented. Instead, they are included in Figures 37 to 41. The respective accuracies are summarised in Table 18. All five variables, $I_{i,NR}$, $I_{total,NR}$, $\overline{d}$, V_{WR}, and $N_{i,WR}$, closely approximate the shape of the experimental data.

For a discussion on the limitations and derivation of the NR intrusion count model, the reader is referred to Appendix F.2. For the mean delay, the analytical model overestimates the experimental data. In the discussion of Appendix B, this overestimation was predicted at unbalanced intersections due to an overestimation of the red time (see Section 7). In the orthogonal grid network, multiple unbalanced intersections exist (as shown in Appendix D.3), clarifying the overestimation. The mean velocity and the mean density with conflict resolution are both direct derivatives of the mean delay and, therefore, share the conclusion of the impact of the red time overestimation.

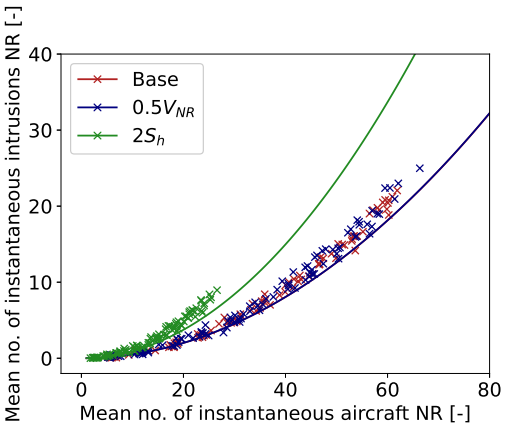

Figure 37: Comparison between the analytical model (solid line) and the fast-time simulation experiment (x) for $I_{i,NR}$ for the grid network experiments

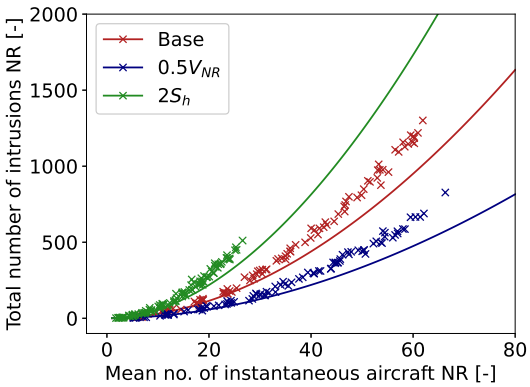

Figure 38: Comparison between the analytical model (solid line) and the fast-time simulation experiment (x) for $I_{total,NR}$ for the grid network experiments

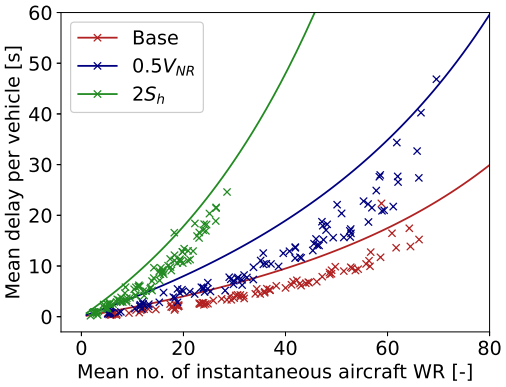

Figure 39: Comparison between the analytical model (solid line) and the fast-time simulation experiment (x) for $\overline{d}$ for the grid network experiments

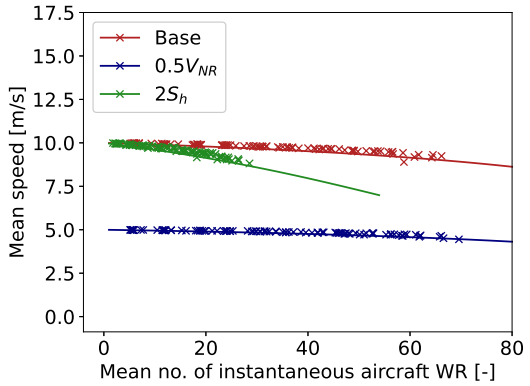

Figure 40: Comparison between the analytical model (solid line) and the fast-time simulation experiment (x) for $\overline{V}_{WR}$ for the grid network experiments

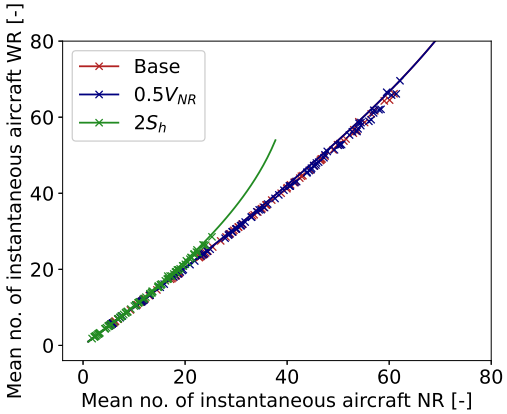

Figure 41: Comparison between the analytical model (solid line) and the fast-time simulation experiment (x) for $\overline{N}_{i,WR}$ for the grid network experiments

Table 18: Accuracy of the specific analytical models for the grid network experiments. Note: $\overline{V}_{WR}$ is not included, as k and $k_{\%}$ are not suitable for this comparison

	Base		$0.5V_{NR}$		$2S_h$	
Variable	k	$k_{\%}$	k	$k_{\%}$	k	$k_{\%}$
$I_{i,NR}$	1.13	88.8%	1.15	87.1%	1.33	75.1%
$I_{total,NR}$	1.25	80.2%	1.34	74.5%	1.32	76.0%
$\overline{d}$	0.68	52.9%	0.68	52.3%	0.69	55.4%
$\overline{N}_{i,WR}$	0.979	97.9%	0.978	97.7%	0.974	97.3%